AIAA JOURNAL
Vol. 55, No. 12, December 2017

Effect of Impinging Wake Turbulence on the Dynamic Stall of a Pitching Airfoil

Brandon E. Merrill* and Yulia T. Peet†
Arizona State University, Tempe, Arizona 85287

DOI: 10.2514/1.J055405

Dynamically moving airfoils are encountered in helicopter rotors, wind-turbine blades, and maneuvering aircraft. A clearer understanding of how freestream disturbances affect the aerodynamic forces on pitching airfoils leads to improved designs. In the present study, the authors' recently validated spectrally accurate moving overlapping mesh methodology is used to perform a direct numerical simulation of a NACA 0012 airfoil pitching with oscillatory motion in the presence of a turbulent wake created by an upstream solid cylinder. The global computational domain is decomposed into a stationary background mesh, which contains the solid cylinder, and a mesh constructed around the airfoil that is constrained to pitch with predetermined reduced frequency $k = 0.16$. Present simulations are performed with chord-based Reynolds number $Re_c = 44{,}000$. Aerodynamic forces and vortex-shedding properties are compared between the pitching airfoil simulations with and without upstream disturbances. Power spectral density functions of the aerodynamic forces and moments are investigated to further determine the effect of a turbulent wake on a pitching airfoil.

Nomenclature

C = Courant number
C_D = coefficient of drag
C_L = coefficient of lift
C_M = coefficient of pitching moment
c = airfoil chord length
D = drag, and cylinder diameter
f = oscillation frequency
k = reduced pitching frequency
L = lift
$L_{\hat{n}}$ = computational mesh length in the direction
M = pitching moment
P = power from power spectral density function
Re_c = chord-based Reynolds number
Re_D = diameter-based Reynolds number
S = planform area
St = Strouhal number
TI = turbulence intensity
t = time
U_∞ = inflow velocity
u = fluid velocity
V = volume
α = angle of attack
α_m = mean angle of attack
α_a = oscillation amplitude of the angle of attack
Γ = strength of the dynamic stall vortex
Δn = collocation point spacing in the wall-normal direction
Δs = collocation point spacing in the streamwise direction
Δz = collocation point spacing in the spanwise direction
ρ = fluid density
ω = vorticity

I. Introduction

BETTER understanding of the aerodynamic forces acting on airfoils with a wide variety of flow conditions is imperative in creating flexible models to improve the fidelity of large-scale aerodynamic simulations and contribute to more efficient designs. Although many aspects of airfoil aerodynamics have been examined in depth, several facets have traditionally been difficult to measure or simulate. The flow around pitching airfoils is one facet of research that has been studied for several decades, although much is unknown regarding the nature of the flow when unsteady flow conditions are present. The flow around pitching airfoils, especially as it relates to dynamic stall, has ramifications for the efficiency and design of helicopter rotors [1,2], wind turbines [3], other rotating machinery such as compressors [4], as well as extensions to the maneuverability of fixed-wing aircraft [5,6].

The general characteristics of pitching airfoils and mechanisms of dynamic stall are predominantly understood in the presence of steady inflow conditions, and several experimental and computational projects have examined this topic [7–13]. The lift force on a dynamically pitching-upward airfoil with steady inflow will generally increase up to an angle of attack beyond its static stall angle until dynamic stall occurs. As an airfoil pitches upward, a large vortex, referred to as a dynamic stall vortex (DSV), forms at the leading edge of an upward-pitching airfoil, creating a low-pressure region, which then travels along the suction side of the airfoil toward the trailing edge. The lower pressure on the suction side of the airfoil increases the lift, until the vortex nears the trailing edge, where it separates, and a dramatic decrease in lift (dynamic stall) ensues. Dynamic stall research typically focuses on the effects of altering pitching frequency, pitching amplitude, Reynolds number, and Mach number as well as possible ways to gain greater control of dynamic stall [14–19]. However, unsteady inflow conditions can also play a crucial role in the aerodynamics of pitching and plunging airfoils. Turbulence, gusts, and vortices caused by upstream structures, objects, or atmospheric conditions create unsteady inflow for helicopter rotors, wind-turbine blades, and wings on maneuvering aircraft. In addition, these aerodynamic bodies often operate in each other's wakes, such as wind turbines in wind arrays or aircraft in formation flight. To create a more complete realization of dynamic stall phenomena, the upstream velocity fluctuations commonly experienced by pitching airfoils need to be included in future research and simulations.

Although some experimental research regarding unsteady inflow effects on pitching airfoils has been performed, much less computational work has been done in this area due to the difficulty of coupling nonuniform inflow conditions with a dynamic pitching

---

Received 3 December 2016; revision received 17 May 2017; accepted for publication 15 July 2017; published online 31 August 2017.

*Ph.D. Student, School for Engineering of Matter, Transport, and Energy; currently Senior Systems Engineer, Raytheon Missile Systems, Modeling, Simulation, & Analysis, Tucson, AZ 85756.

†Assistant Professor, School for Engineering of Matter, Transport, and Energy.

motion in computational models. In the 1970s, Pierce et al. [2] and Kottapalli and Pierce [20] performed experiments on pitching helicopter blades with cyclic inflow conditions, showing that these inflow conditions affected the forces and moments on the blade with varying magnitudes dependent upon the phase difference between the airfoil oscillation and inflow velocity oscillation. A similar study by Shi and Ming [5,6] investigated a pitching delta wing, for improvements in the design of supermaneuverable aircraft. Recent computational work by Gharali and Johnson [21,22] investigated two-dimensional pitching airfoils with laminar periodic inflow velocity using an unsteady Reynolds-averaged Navier–Stokes solver.

The effect of incoming turbulence on pitching airfoils was first identified in the experiments of Conger and Ramaprian [23], who reported larger magnitudes of pressure and aerodynamic forces in their investigation of a pitching-upward NACA 0015 airfoil than the previous measurements obtained at similar Reynolds numbers, which they attributed to a relatively high freestream turbulence level in their water channel (about 1%). Amandolèse and Széchényi [24] measured lift, pitching moment, and pressure distributions on a section wind-turbine model blade oscillating in stall in the presence of freestream isotropic turbulence generated with a square grid, with turbulence intensity (TI) levels between 1.1 and 7.5%. Leu et al. [25] performed particle image velocimetry (PIV) visualizations of the flowfield around an oscillating pitching NACA 0015 airfoil in the presence of a grid-generated turbulence with intensity of about 7%. Recently, Kim and Xie [26] conducted a computational study of the effect of turbulence on the aerodynamics of a sinusoidally pitching NACA 0012 airfoil using dynamic mesh capabilities of the OpenFOAM with large-eddy simulations (LES). Freestream turbulence was generated using a synthetic approach [27] and featured 5 and 10% TI levels with the length scales of 0.15–0.3 chord lengths. These studies generally report a delay in boundary-layer separation and a smaller separation bubble in the presence of freestream turbulence, and the PIV visualizations in [25] report a significant impact on the vortex dynamics resulting in stall delay. The effect of freestream turbulence on lift coefficient was studied in [23,24,26]; however, no common trends were identified. The lift values were higher with turbulence during the pitch-up studies in [23]; however, the authors of [24,26] found no significant effect of turbulence on the lift coefficient during the upstroke in their studies, but the lift values increased during the downstroke. The increase in lift values was attributed to the suppression of the separation bubble during various parts of the pitching cycle.

These previous studies have considered effects of isotropic turbulence on the dynamics of pitching airfoils. Although a useful conceptualization, isotropic turbulence is rarely encountered in realistic flows. This study is devoted to investigating the effect of wake turbulence on a pitching airfoil, which is relevant to situations when upstream structures interfere with the airfoil dynamics, as in wind-turbine arrays, stator–rotor interactions, aircraft wing–body configurations, and formation flight. Wake turbulence is characterized by a high degree of anisotropy, nonuniform mean velocity, and a large-scale unsteadiness represented by von Kármán-type vortices [28]. The only previous publication, to the authors' knowledge, that has examined the effect of wake turbulence on pitching airfoils is the experimental study of Chen and Choa [29], who placed a small cylindrical rod in the flow upstream of the pitching-upward NACA 0012 airfoil and performed measurements of the unsteady forces acting on the airfoil surface. Several vertical positions of the upstream cylinder with respect to the airfoil were investigated. In their experiments, disturbed inflow cases reported delayed stall with stronger effects seen when the cylinder was aligned with the airfoil rather than vertically shifted [29]. Their reported lift and pitching moment curves show shifted peak values at larger angles of attack, with lift plots showing lower slopes and higher maxima before stall with freestream disturbances. Chen and Choa [29] hypothesized that the upstream rod acts like a vortex generator that energizes the boundary layer and delays separation. In their study, although lift, pitching moment, and pressure coefficients were documented, details regarding the vortex dynamics and unsteady flow structures contributing to resulting aerodynamic observations were not revealed.

The physics of dynamic stall is characterized by complex processes of boundary-layer transition, separation, and the formation, subsequent instabilities, and reattachment of the shear layer emanating from the leading edge of the airfoil. Laminar-to-turbulent transition is relatively well understood for the flow above the flat plate, both through modal instabilities via H-type and K-type transitions [30] and via bypass mechanisms [31] as well as through modal instabilities via H-type and K-type transitions [30]. Ovchinnikov et al. [32] studied a transition in a flat-late boundary layer induced by a cylinder wake and reported an early onset of transition in this case, similar in nature to the bypass transition. Mechanisms related to the boundary-layer transition over dynamically pitching or plunging airfoils were discussed in [18,19,33,34], whereas mechanisms related to shear-layer instabilities were highlighted in [18,19,34–36], all without freestream disturbances.

In this paper, we aim to investigate the aerodynamics of pitching airfoils in the presence of an impinging turbulent wake with the goals of understanding how the airfoil vortical systems are modified with the presence of disturbances and how it affects the resulting airfoil performance. Following our preliminary study in [37], we perform direct numerical simulations (DNS) of the NACA 0012 airfoil with a chord Reynolds number of 44,000 oscillating in pitch in a turbulent wake. Several methodologies exist in the literature aimed for a generation of a realistic inflow turbulence; see for example a recent comprehensive review of Wu [38]. They can be roughly divided into synthetic methods, where turbulence is synthesized as random fluctuations obeying some specified correlation laws [27,39,40], or recycling methods, where an inflow turbulence is reintroduced from an already computed turbulent flowfield, in a strong [41] or weak [31,42] manner. A synthetic approach (although some significant advances have been made [38]) still requires a long development section [42,43] and demonstrates strong sensitivities to the input parameters [40]. A recycling approach generally calls for a separate auxiliary simulation for the generation of the inflow turbulence as a "precursor" and is unlikely to offer computational advantages in the current problem. To avoid the aforementioned deficiencies associated with synthetic or recycling turbulence generation approaches, we, as in experimental study of Chen and Choa [29], place a small cylinder upstream of a pitching airfoil and directly compute the turbulent wake shed by the cylinder, in a fully coupled manner with the pitching airfoil simulations. These novel simulations are possible due to our recently developed moving overlapping grid methodology in a spectral-element method that features spectral accuracy in space and high-order accuracy in time and is well suited for high-fidelity simulations on moving domains [44–46].

The paper is organized as follows. In Sec. II, we describe the problem setup of the pitching airfoil simulations investigated. Section III presents an overview of the computational methods used, including our spectrally accurate moving overlapping mesh solver. Section IV presents the results of our turbulent wake validation and the airfoil simulations with and without the turbulent wake, focusing on the correlation between the unsteady flow structure and the aerodynamic coefficients. In Sec. V, we document the power spectral density analysis of the lift, drag, and pitching moment. A discussion of major findings and description of future work is presented in Sec. VI.

II. Problem Setup

The present project simulates a NACA 0012 airfoil with oscillatory pitching motion and chord-based Reynolds number $Re_c = 44{,}000$. We investigate its interactions with a turbulent wake generated by a small stationary cylinder, with diameter-based Reynolds number $Re_D = 3900$, that disturbs the upstream flow. We investigate and compare three cases as presented in Table 1. Case 1 corresponds to steady inflow (without a cylinder wake), which will serve as the baseline case and provide opportunities for validation with the previous experimental results [47]. Cases 2 and 3 investigate the effects of upstream disturbances on the pitching airfoil, where a cylinder, in case 2, is positioned at the same vertical position as the airfoil pitching

Table 1 Pitching airfoil cases (c is the airfoil chord-length)

Case	Position of cylinder $(x/c, y/c)$	Position of airfoil quarter-chord $(x/c, y/c)$	k	α_m, deg	α_a, deg
1	No cylinder	(1.2, 0)	0.16	15.3	9.7
2	(0, 0)	(1.2, 0)	0.16	15.3	9.7
3	(0, −0.15)	(1.2, 0)	0.16	15.3	9.7

Table 2 Grid resolution at the solid surfaces

Surface	$\Delta s_{U\,\max}/c$	$\Delta s_{L\,\max}/c$	$\Delta n_{\min}/c$	$\Delta z_{\min}/c$	$\Delta z_{\max}/c$
Airfoil	6.4×10^{-3}	9.0×10^{-3}	4.5×10^{-5}	1.7×10^{-3}	4.7×10^{-3}
Cylinder	2.0×10^{-3}	NA	1.3×10^{-4}	1.5×10^{-3}	4.3×10^{-3}

Table 3 Grid resolution at the solid surfaces in "plus" units

Surface	$\Delta s^+_{U\,\max}$	$\Delta s^+_{L\,\max}$	$\Delta n^+_{\min}$	$\Delta z^+_{\min}$	$\Delta z^+_{\max}$	N_v
Airfoil	28.16	39.60	0.20	7.48	20.68	11
Cylinder	8.80	NA	0.57	6.60	18.92	6

axis, and in case 3, the cylinder's position is shifted vertically down. Thus, in case 2, disturbances impact directly on the leading edge of the airfoil for most of the pitching cycle, and in case 3, the effect of disturbances is mostly confined to the pressure side of the airfoil. We can categorize case 2 as a stronger disturbance with respect to a steady inflow as compared to case 3.

Modeling the interaction of a cylinder wake with the airfoil pitching motion is performed with our recently developed high-order dynamic overset grid methodology outlined in the next section. Two meshes are used in the simulations: an inner airfoil mesh prescribed to move with the airfoil pitching motion, and an outer background stationary mesh, which either contains or does not contain a fixed solid cylinder inside. Overlapping meshes used to perform these simulations are shown in Fig. 1.

In all three cases, the global domain has streamwise, vertical, and spanwise lengths of $L_x/c = 10$, $L_y/c = 6$, and $L_z/c = 0.2$, respectively, where c is the airfoil chord length. The inner airfoil mesh is the same for all the cases, with grid spacings at the airfoil surface given in Table 2, and contains ~54,000 elements (~19 million degrees of freedom). Table 2 presents the maximum streamwise collocation point spacing on the upper ($\Delta s_{U\,\max}/c$) and lower ($\Delta s_{L\,\max}/c$) surfaces of the airfoil (lateral spacing in the case of the cylinder; note that, because of nonuniform GLL point distribution, minimum spacing is about three times less and the average spacing is about twice less), normal spacing for the first grid point from the wall on the upper airfoil surface at the midchord location and at the cylinder surface ($\Delta n_{\min}/c$), and the minimum ($\Delta z_{\min}/c$) and maximum ($\Delta z_{\max}/c$) spanwise collocation point spacing. The airfoil mesh was ensured to satisfy typical DNS grid resolution requirements, as can be seen in Table 3. Although grid resolution for DNS is usually judged by the mesh resolution in "plus" units that are related to local skin friction velocity [48], it is difficult to provide these estimated for a dynamic stall problem because skin friction at the airfoil surface varies significantly throughout the cycle (see typical plots of skin friction at different angles of attack in Fig. 16). Nonetheless, for the completeness of discussion, we document the plus values for the airfoil mesh based on a reference value of $C_f = 0.02$, which is rarely exceeded, in Table 3 (the notation is the same as in Table 2; N_v is the number of collocation points within the viscous sublayer).

For the disturbed airfoil inflow cases, an outer background mesh contains an upstream cylinder with the diameter of $D \approx c/11.25$ triggering the disturbances. The horizontal distance from the center of the cylinder to the pitching axis of the airfoil located at the quarter-chord position is $L_x = 1.2c$, or, in terms of cylinder diameters, $L_x \approx 13.5D$. In case 2, the center of the upstream cylinder is on the same horizontal plane as the quarter-chord axis of the airfoil, and in case 3, the cylinder is shifted down by $0.15c$, or $1.6875D$. The background mesh contains ~16,000 elements (~3.4 million degrees of freedom) for case 1 and ~21,000 elements (~4.5 million degrees of freedom) for cases 2 and 3 due to the addition of the cylinder. The mesh resolution at the cylinder surface is documented in Tables 2 and 3 as well, whereas the value of skin friction $C_f = 0.02$ was used again for the calculation of plus units, which happens to be a typical value for the cylinder surface as well.

The NACA 0012 airfoil was constrained to move with an oscillatory pitching motion about its quarter-chord axis prescribed as

$$\alpha = \alpha_m - \alpha_a \cos(2\pi f t) \tag{1}$$

where α is the angle of attack, $\alpha_m = 15.3$ deg is the mean value, $\alpha_a = 9.7$ deg is the oscillation amplitude, and the frequency f is expressed in terms of the nondimensional reduced frequency $k \equiv \pi f c/U_\infty = 0.16$.

For the global (outer) domain, we prescribe a steady uniform velocity U_∞ on the far-left boundary, outflow conditions on the right boundary, and symmetry conditions on the top and bottom boundaries. Periodic conditions are prescribed on the spanwise boundaries. The left, top, and bottom boundaries of the inner (airfoil) mesh use interface conditions to pass values between subdomains, as described in the next section, whereas the right boundary is prescribed outflow conditions for a smooth propagation of shed vortices across the interface. Moving wall boundary conditions with fluid velocity matching the airfoil velocity are prescribed at the surface of the airfoil.

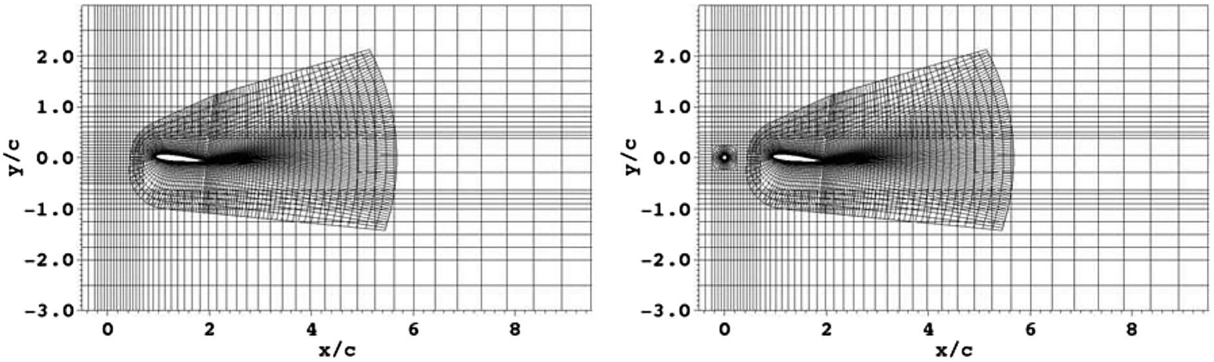

a) Steady airfoil inflow (Case I)

b) Disturbed airfoil inflow with an upstream cylinder (Case II)

Fig. 1 Mesh configurations used in the current simulations of an oscillating airfoil. Only element boundaries are shown.

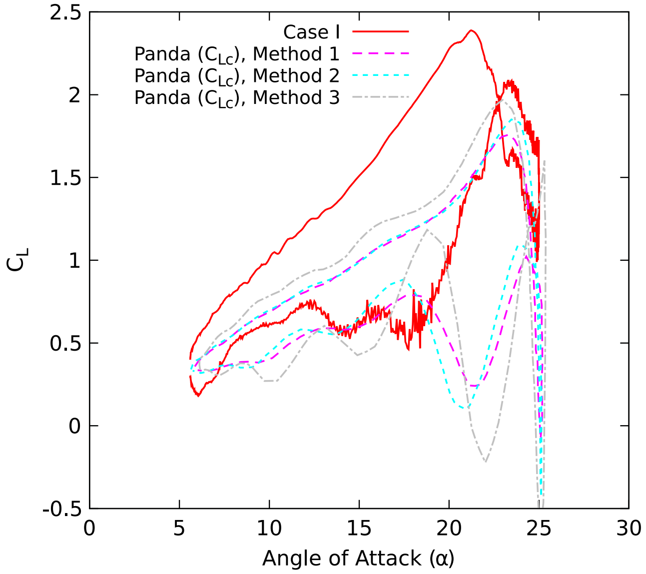

Fig. 2 Lift coefficients from present tests phase averaged over the last five cycles as compared with experimental results of Panda and Zaman [47]. $\alpha_m = 15.3$ deg, $\alpha_a = 9.7$ deg, $k = 0.16$.

III. Methods

Direct numerical simulations in present investigations are performed with the open-source high-order fluid dynamics solver Nek5000 [49], which uses the spectral element method (SEM) for spatial discretization and allows for up to third-order temporal discretization for solutions to the incompressible Navier–Stokes equations. Spatial discretization is performed by dividing each subdomain into a set of elements wherein the solution is approximated using polynomial basis functions that pass through collocation points with Gauss–Lobatto Legendre (GL) point distribution for velocity and Gauss Legendre (G) point distribution for pressure. Exponential spatial convergence is achieved with polynomial order refinement, which thus increases the number of GL and G points defined within each element [44,50,51].

The dynamic interaction of unsteady turbulent wake with the pitching airfoil is handled by using the moving overlapping mesh methodology recently implemented in Nek5000 solver [44–46]. Subdomain movement is handled with the arbitrary Lagrangian–Eulerian (ALE) formulation that has been previously shown to be an efficient method for representing the relative motion of the fluid particles with respect to an arbitrarily moving mesh [46,50,52,53]. Although other approaches for modeling the pitching airfoil motion are possible, such as deforming meshes [54] or sliding meshes [55], the current methodology offers a flexibility to handle high-amplitude pitching and more general motions without the detrimental effects of mesh distortion or the need for remeshing in two- and three-dimensional simulations. The moving overlapping mesh methodology has previously been shown to maintain this exponential spatial accuracy in the global computational domain and was thoroughly validated [44–46]. Parallel computations achieve linear scaling to thousands of processors [44,46].

Within the formulation, a global domain is decomposed into two overlapping subdomains. The mesh in the subdomain that is constrained to move is prescribed a predetermined mesh velocity (corresponding to a motion of a pitching airfoil in our case). Dirichlet velocity conditions are enforced on the moving solid boundaries that match the velocity of the moving rigid body. Values at mesh

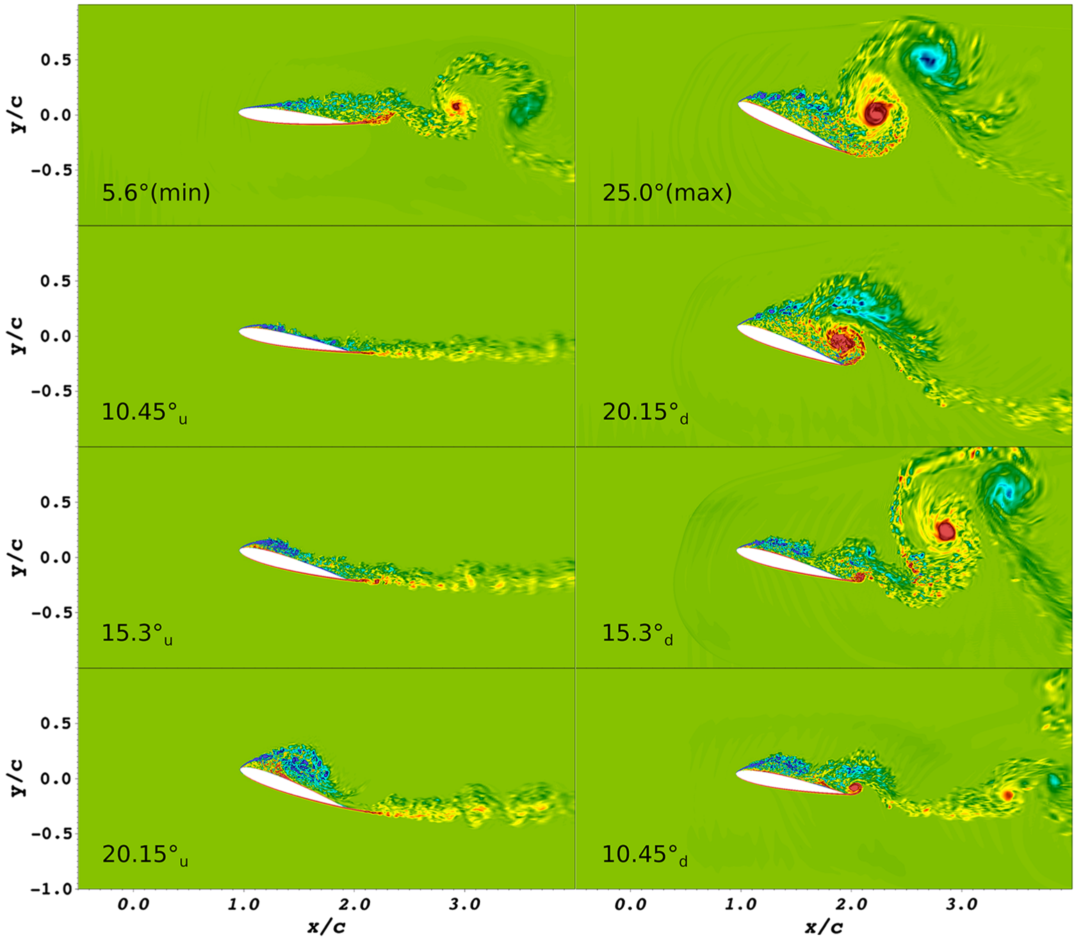

Fig. 3 Zoomed-in spanwise-averaged spanwise vorticity plots during the third cycle, at angles of attack posted. The subscript *u* denotes upstroke, and *d* is downstroke.

interfaces are determined by performing Lagrangian interpolation on values in the adjacent subdomain from previous time steps. This interpolation method, when coupled with the SEM solver, gives spectrally accurate values at collocation points on interface boundaries. Search and locate procedures are carried out to express the location of a point on the interface of one subdomain in terms of the local coordinates of a corresponding element in the other subdomain. Temporal coupling at interfaces is achieved using up to a third-order explicit interface extrapolation scheme (IEXT3), using interpolated values from previous time steps [44,56].

Dynamic time stepping procedure was developed for the moving multidomain simulations to ensure that sufficient temporal resolution is achieved while allowing efficient use of computational resources. Our dynamic time stepping method takes the mesh motion into account when calculating the Courant number for ALE simulations:

$$C_{\mathrm{ALE}} = \max_i |C_{x_i,\mathrm{ALE}} + C_{y_i,\mathrm{ALE}} + C_{z_i,\mathrm{ALE}}| \tag{2}$$

where i enumerates all GL collocation points in the domain. The Courant number for each coordinate direction is calculated:

$$C_{x_i,\mathrm{ALE}} = \frac{u_{i,\mathrm{rel}} \cdot \Delta t}{\Delta x_i} \tag{3}$$

and the relative velocity $u_{i,\mathrm{rel}}$ is calculated using the corresponding fluid velocity (u_i) and mesh velocity ($u_{i,\mathrm{mesh}}$) components at a GL

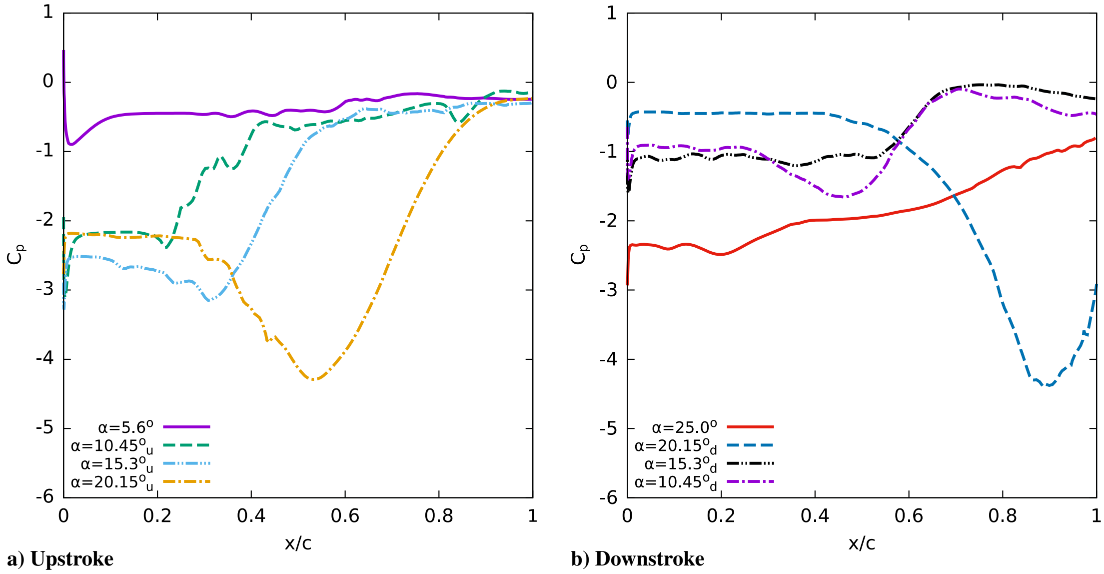

a) Upstroke **b) Downstroke**

Fig. 4 Pressure coefficient values along the suction surface of the airfoil at posted angles of attack during the third pitching cycle. The pressure coefficient values are averaged in the spanwise direction.

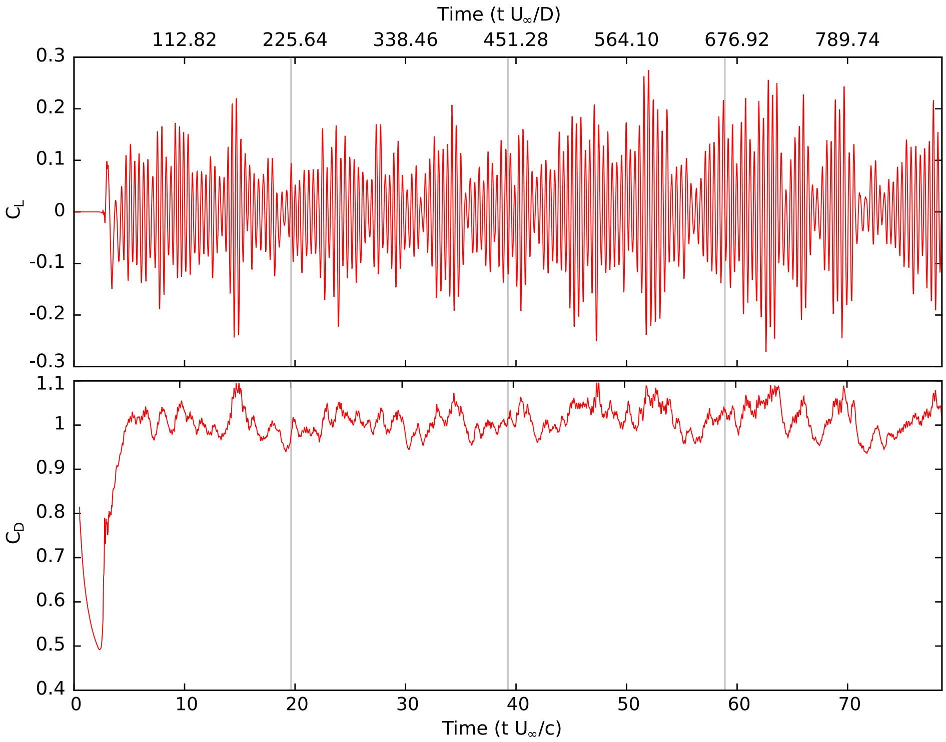

Fig. 5 Time history of force coefficients on a cylinder at $Re_D = 3900$. The bottom axis displays time nondimensionalized with the airfoil chord length and the top axis with the cylinder diameter.

point i, where Δx_i is the characteristic stencil size in the corresponding direction:

$$u_{i,\mathrm{rel}} = |u_i - u_{i,\mathrm{mesh}}| \tag{4}$$

Because the simulations are composed of two subdomains, the maximum Courant number between the subdomains is determined and communicated at each time step. When the maximum Courant number goes above 0.92 or below 0.65, the time step is modified to keep the Courant number within the bounds, to yield computational efficiency while also providing stability. This procedure ensures that both subdomains time-advance with the same time-step size.

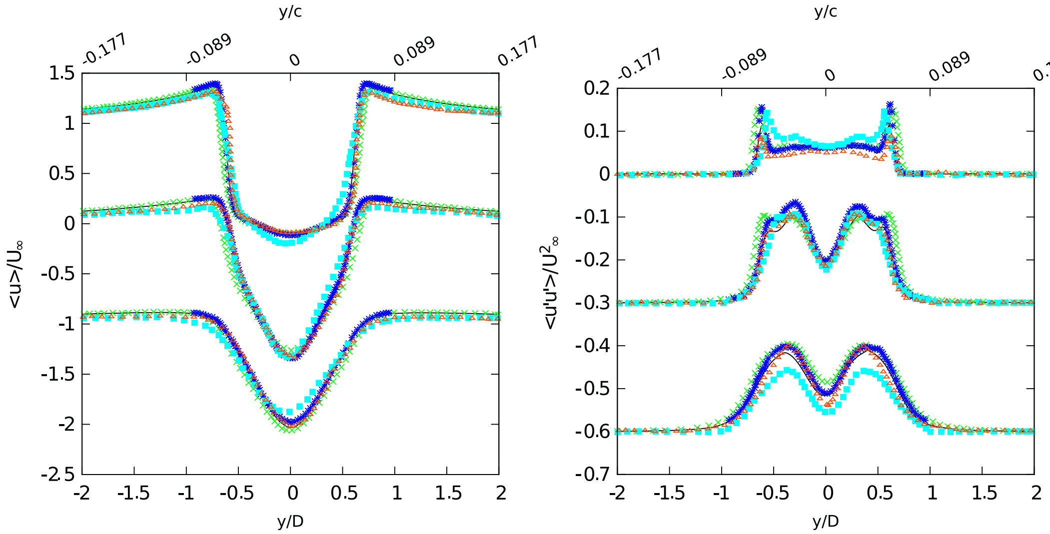

Fig. 6 Validation of the turbulent wake statistics for the flow behind the cylinder at $Re_D = 3900$, averaged over $tU_\infty/D \approx 100$. Streamwise locations 13 $x/D = 1.06$ (top curve), 1.54 (middle curve), 2.02 (bottom curve).

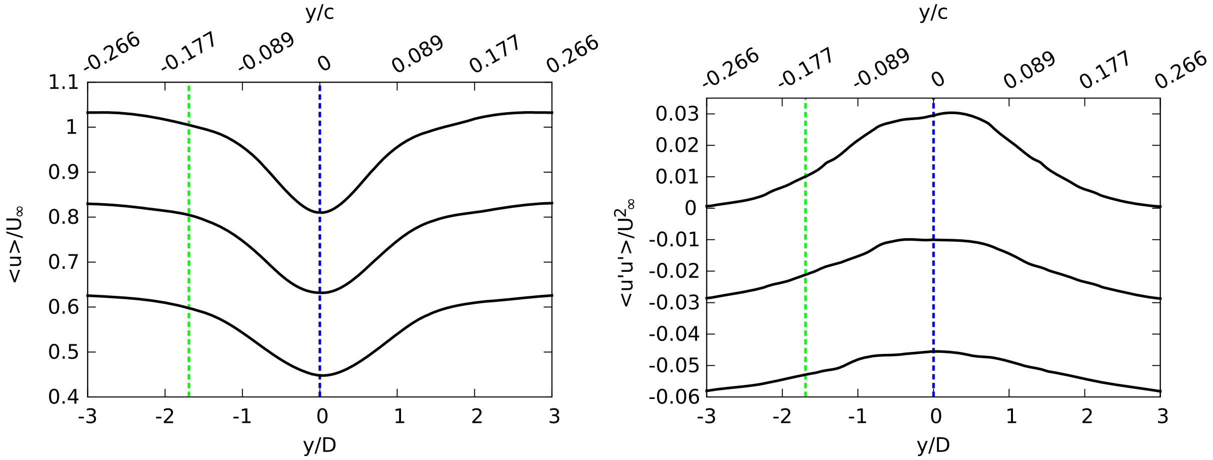

a) Mean streamwise velocity

b) Variance of streamwise velocity

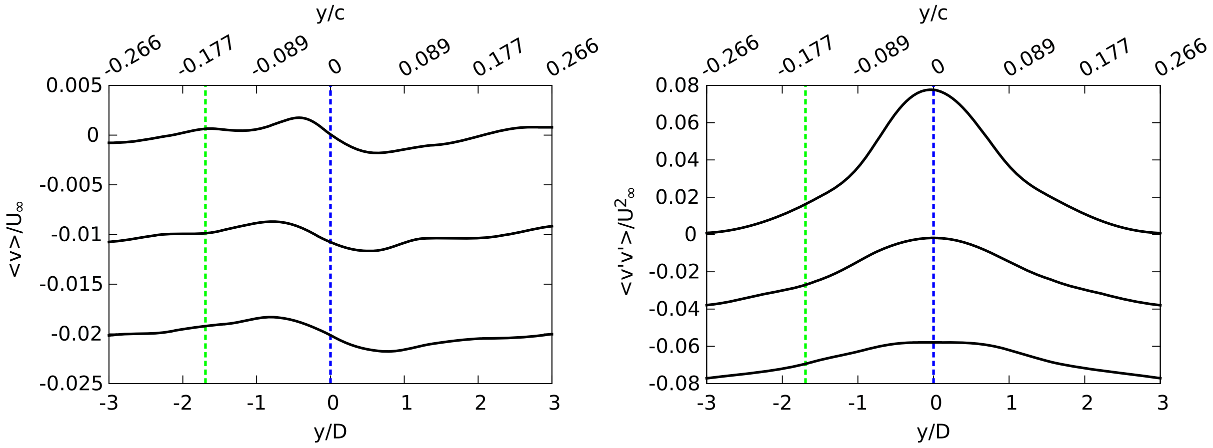

c) Mean vertical velocity

d) Variance of vertical velocity

Fig. 7 Turbulent wake statistics of the flow behind a cylinder at $Re_D = 3900$ at streamwise locations $x/D = 10.7$ (top curve), 16.4 (middle curve), and 22.0 (bottom curve).

Pitching airfoil simulations are performed using sixth-order polynomial approximations for spatial discretization within each element and dynamic time stepping with a maximum time step of $\Delta t_{\max} U_\infty / c = 2 \times 10^{-4}$. The average time step in the simulations was approximately $\Delta t_{\mathrm{avg}} U_\infty / c \approx 5 \times 10^{-5}$. Using the airfoil chord length, freestream velocity, and fluid viscosity, we estimate the eddy turnover time for the smallest scale of turbulent eddies in the calculations (Kolmogorov time scale [57]) to be 4.8×10^{-3} time units, giving, on average, ~100 time steps per eddy turnover time of the smallest, dissipative eddy, thus resolving the temporal characteristics of the turbulent flow. Simulations use second-order time integration with IEXT2 at interface boundaries and two intergrid iterations per time step. All cases were run for six airfoil oscillation cycles and took about 1000 h to complete on 1000 processors on both the San Diego Supercomputer Center Comet and Texas Advanced Computing Center Stampede clusters.

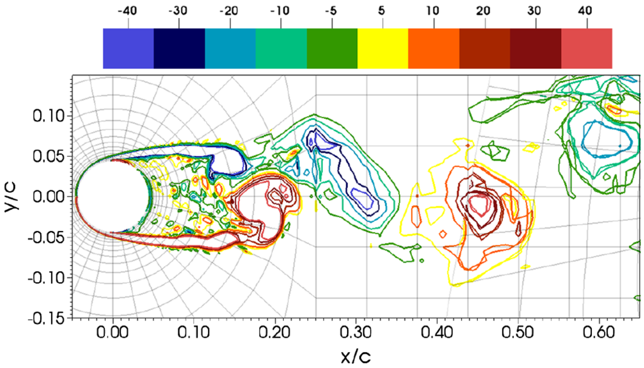

Fig. 8 Zoomed-in spanwise vorticity contours showing both a portion of the cylinder mesh and an interface with the airfoil mesh for case 2 (element boundaries shown). $\alpha_m = 15.3$ deg, $\alpha_a = 9.7$ deg, $k = 0.16$.

IV. Results

In the following sections, the aerodynamic coefficients of lift, drag, and pitching moment acting on the airfoil are calculated as

$$C_L = \frac{L}{(1/2)\rho U_\infty^2 S} \tag{5}$$

$$C_D = \frac{D}{(1/2)\rho U_\infty^2 S} \tag{6}$$

$$C_M = \frac{M}{(1/2)\rho U_\infty^2 Sc} \tag{7}$$

where L is the lift force, D is the drag force, M is the pitching moment (or torque), ρ is fluid density, U_∞ is the inflow velocity, S is the planform area, and c is the chord length.

A. Oscillating Airfoil with Steady Airfoil Inflow

In this section, we discuss the results of case 1, which are used as a baseline for comparison with the two unsteady airfoil inflow cases.

1. Validation

For the validation, simulation results are compared with the experimental results of Panda and Zaman [47]. This experimental data set was chosen because it used the same Reynolds number $Re_c = 44{,}000$ as in the current study, which is feasible for a DNS of

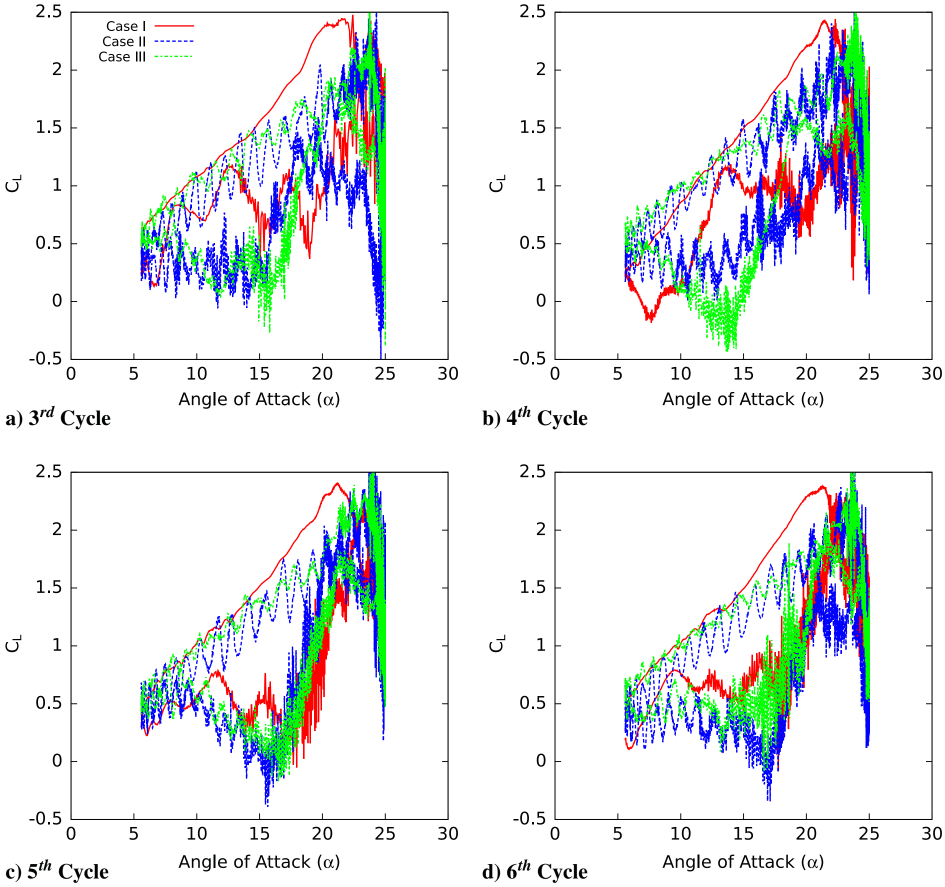

a) 3rd Cycle

b) 4th Cycle

c) 5th Cycle

d) 6th Cycle

Fig. 9 Lift coefficient results compared among all three cases for the third through sixth cycles. $\alpha_m = 15.3$ deg, $\alpha_a = 9.7$ deg, $k = 0.16$.

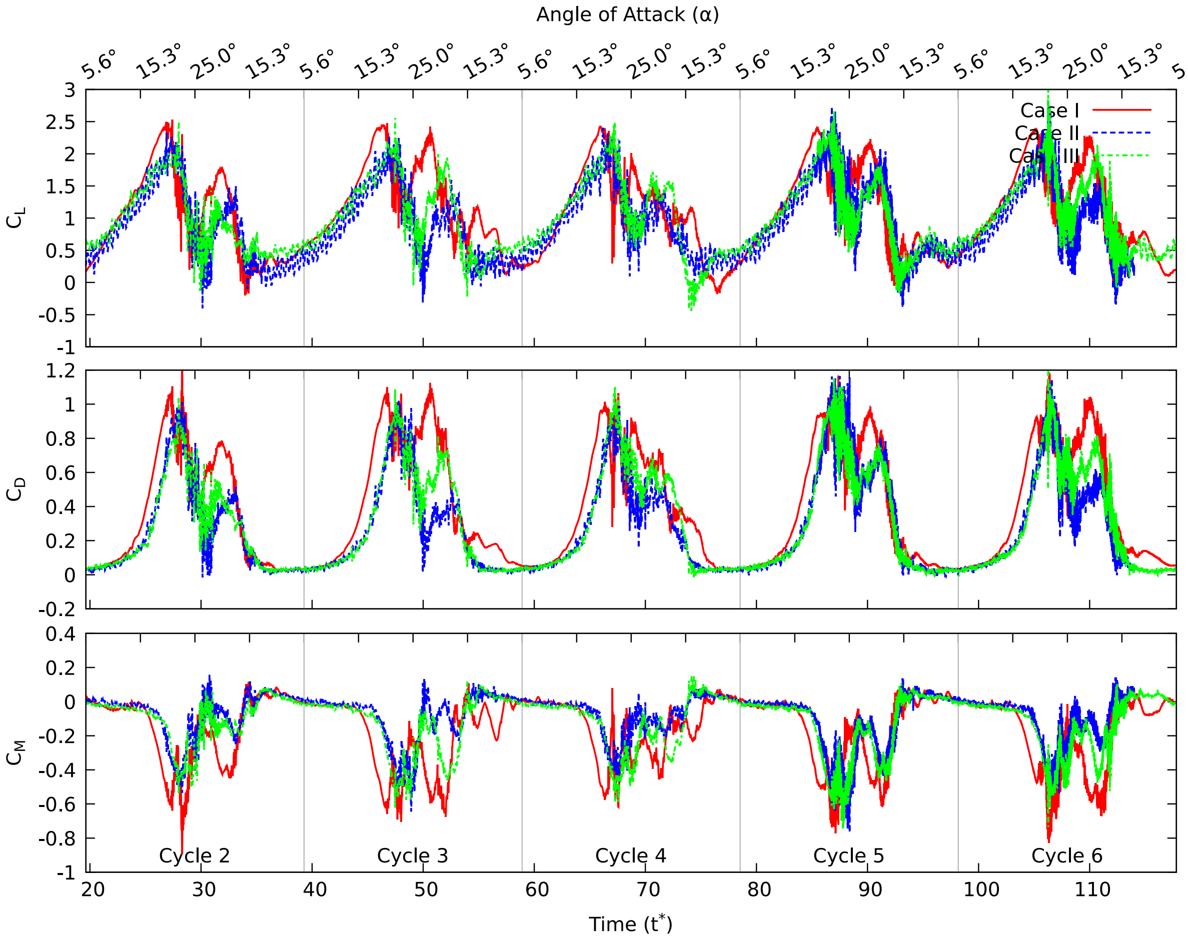

Fig. 10 Aerodynamic forces and moments for cases 1, 2, and 3 for the last five cycles. Time (tU_∞/c) along the bottom axis, and corresponding angle of attack along the top axis.

the flow and was difficult to find elsewhere in experiments on pitching airfoils. In [47], hot-wire probes were used in the wake of an oscillating airfoil to collect velocity and vorticity data of the flow in the wake. The unsteady lift force, reported in [47], is divided into a noncirculatory component and a circulatory component [58], where Panda and Zaman used the experimental wake data to approximate only the circulatory component of the lift force acting on the airfoil. They argued that, although the addition of the noncirculatory component would change the values of the total lift force, the difference is fairly minor and even negligible at small reduced frequencies [47]. In the present simulations, the total lift coefficient values are compared with only the circulatory component of lift that is published in [47].

Three methods are described in Panda and Zaman [47] for approximating the circulatory component of lift by integration of the phase averaged measured vorticity data. We would like to note that the reference value of the circulatory lift component is not known in their methodology because an unknown steady contribution to the lift approximation exists due to vortices shed before the start of data collection. Because this unknown steady contribution does not vary with the angle of attack, it simply represents an upward or downward shift in the data, and the general shape of the curve showing the variation with the angle of attack and hysteresis should still be appropriately captured. To compare experimental results with our data, this arbitrary shift in the experimental data was calculated to match the phase-averaged lift value in present simulations at the minimum angle of attack. The match at the minimum angle of attack was chosen due to a lowest probability of error in lift value in both simulations and experiments at this relatively simple flow state when the boundary layer and the shear layer are mostly laminar and attached, and vortical systems at the airfoil surface have been yet been formed.

In Fig. 2, present simulation data phase averaged over the last five out of six total cycles are compared with the experimental data [47], which were phase averaged over 80 cycles. In experiments, however, an instantaneous datum at a single spanwise location was obtained and phase averaged, whereas in the simulations, an additional averaging in a homogeneous spanwise direction was performed, over 61 computational planes, before phase averaging. We see that, although the general shapes of the curves in the simulation and experiment are the same, the present simulation data report higher lift values than the experimental approximation, and though lift values during downstroke (the lower curves) do not exactly follow the experimental approximations, the same features are present, namely a local minimum near the maximum angle of attack $\alpha = 25$ deg followed by an increase in lift at the downstroke, and then another stall event. Following the major stall event during the downstroke, the lift values oscillate, in both simulation and experimental data, until the airfoil reaches its minimum angle of attack, $\alpha = 5.6$ deg, after which the next cycle begins. A quantitative disagreement can potentially be attributed to an effect of blockage in the experiments, as further discussed later.

Table 4 Comparison of lift coefficient maxima during the third cycle among all three cases

	Third cycle		
Parameter	Case 1	Case 2	Case 3
Maximum C_L	2.623	2.596	2.576
Time of $C_{L,\max}$ (tU_∞/c)	46.735	47.890	47.485
α of $C_{L,\max}$	22.4°_u	24.3°_u	23.8°_u
Secondary maximum C_L	2.426	1.593	1.947
Time of $C_{L,\max_2}$ (tU_∞/c)	50.630	52.540	52.204
α of $C_{L,\max_2}$	23.8°_d	19.7°_d	20.6°_d

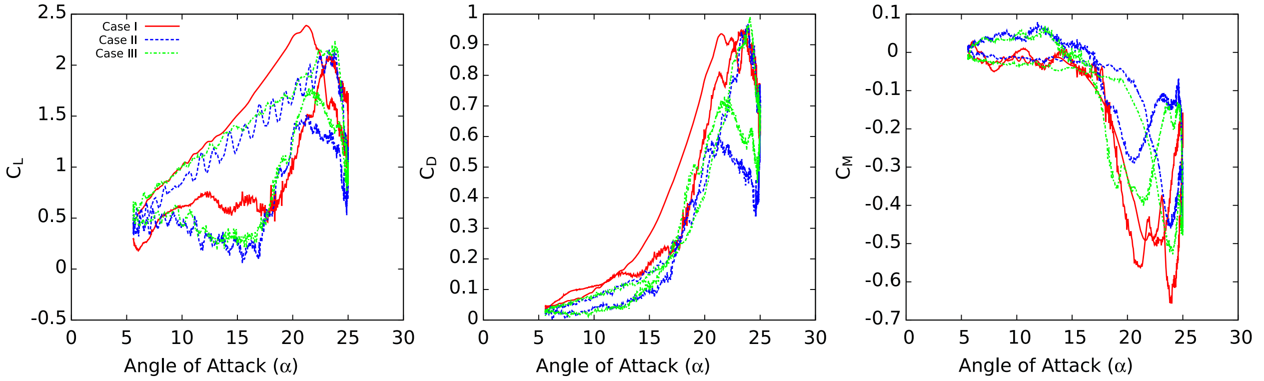

a) Lift coefficient b) Drag coefficient c) Pitching moment coefficient

Fig. 11 Comparison of aerodynamic forces and moments phase averaged over the last five cycles for cases 1, 2, and 3.

2. *Physics of Dynamic Stall*

Here, we further investigate the physics of dynamic stall by performing flow visualizations and correlating the vortex dynamics observed in the flowfield with the pressure coefficient values, at different angles of attack, to be later compared with the disturbed airfoil inflow cases.

Visualizations of the spanwise-averaged spanwise vorticity (Fig. 3, where darkest blue represents spanwise vorticity of less than $\omega_z U_\infty / c = -40$, corresponding with clockwise fluid motion, and darkest red is greater than $\omega_z U_\infty / c = 40$, corresponding with counterclockwise fluid motion) at different angles of attack show the clockwise rotating dynamic stall vortex (DSV) forming at the leading edge and traveling toward the trailing edge as the airfoil pitches upward. In the $\alpha = 15.3^\circ_u$ frame, we find evidence of the boundary layer beginning to separate at the leading edge of the airfoil, which leads to the formation of a DSV seen in the $\alpha = 15.3^\circ_u$ frame. As the DSV nears the trailing edge, a counterclockwise trailing-edge vortex (TEV) forms, which appears in the $\alpha = 25$ deg frame. When the airfoil begins its downstroke, another clockwise vortex forms at the leading edge, which is smaller than the original DSV, and travels along the upper surface of the airfoil until it detaches, creating a secondary TEV and causing another stall event.

By comparing the pressure coefficient values along the upper surface of the airfoil (Fig. 4) with the spanwise vorticity (Fig. 3) plot, we see that the position of low-pressure valleys correlates with the location of vortex centers. Evidence of the forming DSV is found in the $\alpha = 10.45^\circ_u$ curve by the low pressure at the leading edge of the airfoil. The low-pressure region becomes stronger and propagates toward the trailing edge of the airfoil in the $\alpha = 15.3^\circ_u$ and $\alpha = 20.15^\circ_u$ curves. When the airfoil reaches its maximum angle of attack, the DSV and subsequent TEV have already detached. The $\alpha = 20.15^\circ_d$ curve shows evidence of a TEV resulting from the second major vortex system. After the second major vortex detaches, the pressure values along the suction side of the airfoil begin to normalize to a relatively constant value as the boundary layer reattaches at lower angles of attack.

Table 5 Time-averaged values of the aerodynamic force and moment coefficients (the averaging was performed over the last five cycles of the simulation)

Parameter	Value
Case 1	
C_L	1.1179
C_D	0.3954
C_M	-0.1703
Case 2	
C_L	0.9179
C_D	0.2755
C_M	-8.1689×10^{-2}
Case 3	
C_L	1.0253
C_D	0.3032
C_M	-0.1237

B. Oscillating Airfoil with Disturbed Airfoil Inflow

1. *Cylinder Wake Turbulence*

In this section, we document the characteristics of the turbulent wake produced by the upstream cylinder. To assess the wake characteristics unaltered by the presence of the airfoil, and for the validation, a separate direct numerical simulations of a three-dimensional circular cylinder with diameter-based Reynolds number $Re_D = 3900$ was performed, which is the same Reynolds number as in the coupled cylinder–airfoil simulation cases described later. DNS simulations of a single cylinder are performed using sixth-order polynomial approximations and a fixed time step $\Delta t U_\infty / c = 5 \times 10^{-5}$. The mesh has characteristics similar to the background mesh in the coupled simulations and is described in detail in [59].

In pitching airfoil simulations, the airfoil begins pitching upward at $t = 0$, the same time as the cylinder simulations start from steady initial conditions, and thus the first cycle will serve to give the turbulent wake time to fully develop. The time history of the lift and drag forces acting on the cylinder is illustrated in Fig. 5, where gray lines denote the times at which new oscillation cycles begin in oscillating airfoil simulations. The unsteady effects on the cylinder are fully developed before $tU_\infty / c = 10 (tU_\infty / D \approx 112.82)$, allowing a sufficient time for the unsteady effects to propagate into the cylinder wake, where the airfoil will be located, before the second cycle begins.

The turbulent statistics for the wake behind the cylinder (without an airfoil) were thoroughly validated versus previously published computational and experimental data [60–65] in [59]. Good agreement was obtained in the mean and variance values of streamwise and vertical velocities in the near wake ($x/D = 1.06, 1.54, 2.02$) and far wake ($x/D = 6.0, 7.0, 10.0$) locations (only streamwise velocity in the near wake is shown here in Fig. 6 for present (—), LES [62] (×), PIV [62] (∗), B-spline [63] (■), and DNS [64] (△) data; the rest of the validation data are readily accessible in [59]). Note that in Figs. 6 and 7 the middle and bottom curves have been shifted according to the conventions in [63]. In addition, the vortex-shedding frequency was validated as well, giving in the present simulation a Strouhal number $St \equiv fD/U_\infty = 0.216$, which agrees well with the experimental data of the same case presented by Cardell [66], which finds a Strouhal number of $St = 0.215 \pm 0.005$.

Although turbulent statistics are not generally collected in the very far wake ($x/D > 10$), it is the region of particular interest in this case because it is the location in the wake where the airfoil will reside. We therefore present in Fig. 7 the mean streamwise and vertical velocities as well as variances at the leading edge, midchord, and trailing edge locations on an airfoil at $\alpha = 0$ deg ($x/D = 10.7, 16.4$, and 22.0, respectively), where the blue (dotted) and green (dashed) vertical lines represent the vertical position of the pitching axis of the airfoil relative to the wake centerline for cases 2 and 3, respectively. Because of low-frequency motions in the very far wake [67,68], a rather long averaging time of $tU_\infty/D \approx 800$ was used in these locations to ensure smooth statistics.

To characterize the structure of the incoming wake turbulence impinging on an airfoil, we estimate the turbulence intensity at $x/D = 10.7$ and $y/D = 0, -1.6875$ (leading edge of the airfoil at $\alpha = 0$ deg in cases 2 and 3) to be ∼18 and ∼9%, respectively, where we define turbulence intensity as $\mathrm{TI} = \sqrt{1/3(\langle u'u'\rangle + \langle v'v'\rangle + \langle w'w'\rangle)}/U_\infty$. The wake half-width d_w defined by the distance from the centerline to the point where the mean streamwise velocity deficit is half of the deficit at the centerline, $U_\infty - \langle u\rangle_{d_w} = 1/2(U_\infty - \langle u\rangle_0)$, at the $x/D = 10.7$ location is about $0.7D$ or $0.06c$.

To further validate the cylinder wake simulations and characterize the vorticity transport in the wake with changing mesh resolution, spanwise vorticity contours are presented in Fig. 8 that illustrate minimal numerical dissipation of the wake vortices propagating from fine to a coarser mesh. Figure 8 additionally includes the interface with the inner airfoil mesh for the coupled simulations of case 2 showing a smooth transition of the wake vortices across the background inner mesh interface. Additional test cases confirming that minimal errors are incurred at the mesh interfaces in the present high-order moving overlapping grid methodology can be found in [44,46].

2. *Pitching Airfoil in a Turbulent Wake*

In this section, we discuss cases 2 and 3, which correspond to turbulent wake inflow cases. In case 2, the center of the upstream cylinder generating the freestream disturbances is placed on the same horizontal plane as the quarter-chord axis of the airfoil, and in case 3, the center of the cylinder is $0.15c$ lower than the airfoil quarter-chord axis. The mesh for case 2 is presented in Fig. 1b, where a similar mesh is used for case 3 with a shifted cylinder. The general description of the problem setup is done in Sec. II.

In the coupled cylinder–airfoil DNS, the airfoil pitching simulations and the cylinder wake simulations are done concurrently, and the airfoil begins its first cycle at initially steady flow at time zero, before the cylinder wake has developed. It was ensured that the cylinder turbulent wake is fully developed for the entire region wherein the airfoil resides before the beginning of the second cycle. The following discussion will thus focus on the last five cycles of the airfoil motion (although the first cycle is often shown for completeness).

A comparison of the lift coefficient loops among the three cases for the third through sixth cycles (Fig. 9) shows stark differences in the lift that the airfoils experience in each case. The lift acting on the airfoil in cases 2 and 3 during upward pitching (top curves) is quite oscillatory due to the incoming wake vortices shed from the upstream cylinder. However, note that the oscillations of lift values in case 3 are not as large as those displayed by case 2 because, in case 3, the vortices are not directly incident upon the leading edge of the airfoil, but slightly below it. We see that, in case 1, the lift increases at a slightly steeper rate starting at $\alpha \approx 15^\circ_u$, which corresponds to the formation of the DSV and its path along the upper surface of the airfoil. In cases 2 and 3, we do not find evidence of a steeper rate of lift increase, and we find that, in the high-lift regions, the lift in case 1 is generally greater than the lift in cases 2 and 3, both at upstroke and downstroke. Judging by the position of the maximum lift peaks and a subsequent drop in lift, we see that dynamic stall occurs earlier (at smaller angles of attack) in case 1 than for the airfoils with turbulent wake inflow. Details on the timing of the dynamic stall in each case will be discussed further.

Figure 10 displays the aerodynamic forces and moments acting on the airfoil in cases 1, 2, and 3 with respect to time. A comparison of lift coefficient maxima during the third cycle is presented in Table 4. We see that $C_{L,\max}$ due to the DSV is comparable among the three cases presented, although the maxima are achieved at different times during the cycle. The secondary maxima of C_L, caused by the secondary

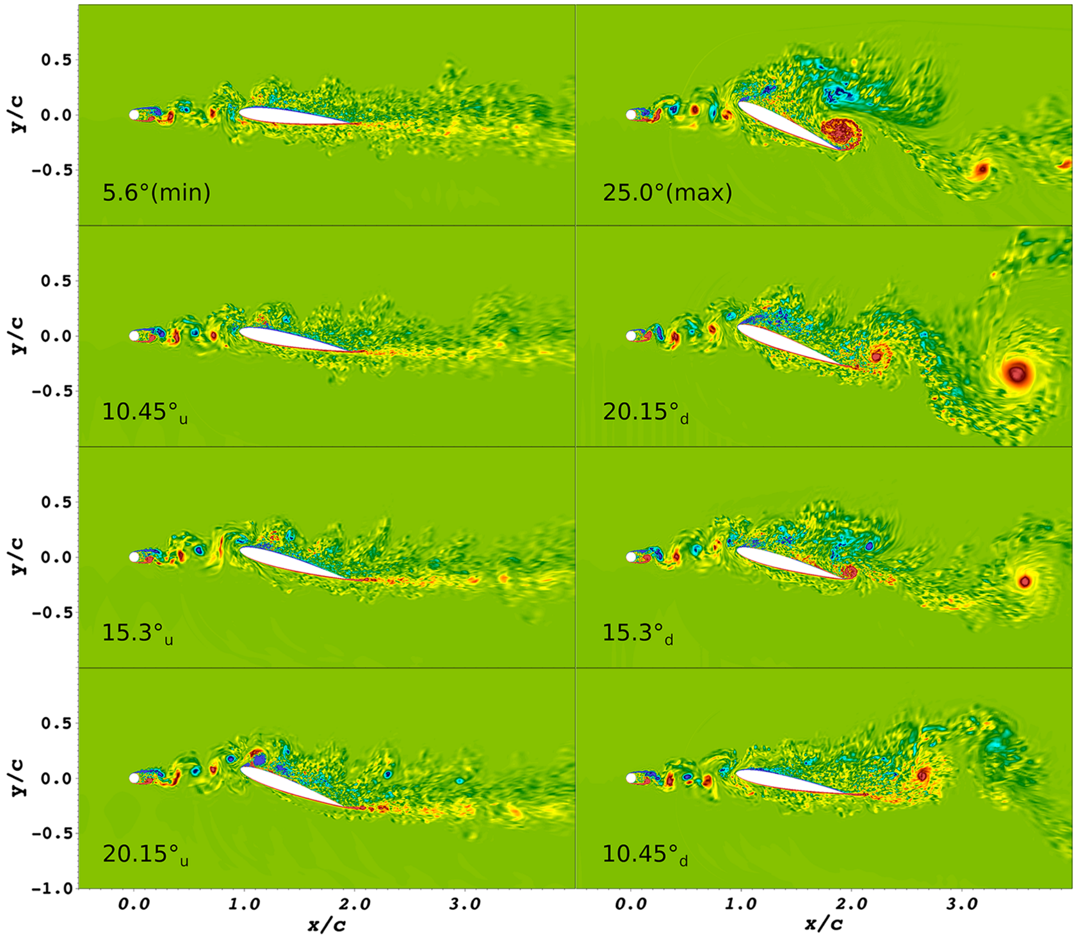

Fig. 12 **Zoomed-in spanwise-averaged spanwise vorticity plots of case 2 during the third cycle, at angles of attack posted.**

vortex formed during downstroke, are noticeably different with case 1 reaching the largest value, followed by case 3, then case 2. This pattern seems repeatable and is found in four out of the last five cycles during the simulation time (refer back to Fig. 10). For both the DSV and secondary vortex, $C_{L,\max}$ is reached earliest in case 1, next in case 3, and last in case 2, and this pattern is also found in the other cycles presented in Fig. 10. We see that incident disturbances have the effect of delaying stall, similar to the experimental findings of Chen and Choa [29], who showed that stall of a constant-rate pitching-upward airfoil occurs at a later time when upstream disturbances are present. Additionally, it appears that larger disturbances incident upon the airfoil's leading edge (such as with inline versus shifted vertical position of the upstream cylinder) have the effect of delaying the stall to a greater extent as well as reducing the value of the secondary lift maximum ($C_{L,\max}$). The data presented here point to the fact that the upstream wake turbulence generated by the cylinder interferes with the airfoil vortical systems associated with the dynamic stall behavior by delaying their formation and weakening their strength, and this interaction is more pronounced for stronger incident disturbances, as in case 2.

Evidence of stall is seen in the drag values as well, with a steep decrease in drag when stall occurs. After initial stall occurs in case 1, a steep increase in drag soon ensues, reaching drag values comparable to the first peak. This second drag peak correlates with the formation of the TEV, and a sharp decrease in drag is again witnessed as the TEV detaches. Cases 2 and 3 do not show clear signs of this large drag peak due to the formation of the TEV. Although the drag acting on the airfoil in the turbulent wake inflow cases nearly reach the same global maximum values as those in case 1 (though at a later time), the drag in nearly all other portions of the cycle is greatly reduced by upstream disturbances, with the larger incident disturbances of case 2 creating a greater drag reduction than case 3. We see particular evidence of this when looking at the drag peak due to the second major vortex formed during the airfoil downstroke in the third cycle, where case 1 reports a local drag maximum of $C_D \approx 1.125$ at $\alpha \approx 23.8^\circ_d$, case 2 reports $C_D \approx 0.512$ at $\alpha \approx 19.5^\circ_d$, and case 3 reports $C_D \approx 0.811$ at $\alpha \approx 22.6^\circ_d$. Other cycles of the simulations show similar patterns for the drag coefficient.

The magnitude of the pitching moment of the airfoil remains small until a large vortex begins to form on the leading edge of the airfoil, where a sharp increase in the magnitude of the pitching moment is seen and continues to increase until the vortex detaches from the surface of the airfoil. In case 1, large fluctuations in the pitching moment are seen for the majority of the cycle, whereas in cases 2 and 3, we see a large fluctuation in the pitching moment as a result of the DSV (though not as large as in case 1), but the pitching moment remains small for the remainder of the cycle. Again, we see that the larger incident disturbances in case 2 diminish the magnitude of pitching moment more so than the offset disturbances of case 3. A comparison of the phase averaged coefficient data (Fig. 11) shows trends for lift, drag, and pitching moment that are in agreement with the previous discussion. An interesting observation from this figure is that the turbulent wake inflow cases show closer agreement in lift coefficient to the experimental results of Panda and Zaman [47] in Fig. 2 than the case 1 with the laminar inflow. Although freestream turbulence was not anticipated in the experiments of Panda and Zaman [47], a maximum blockage of 8.5% occurring at the maximum angle of attack of 25 deg was reported. The effect of blockage on the dynamic stall behavior needs to be further understood, but it can potentially result in similar shifts.

Averages of the aerodynamic coefficient values over the duration of the simulations are given in Table 5. We see that smallest aerodynamic coefficients are found in case 2 followed by case 3 and case 1, aligning with the previous analysis of aerodynamic forces.

To understand the trends observed in the aerodynamic coefficients, we further examine the instantaneous flowfields provided by our simulations. Visual inspection of the spanwise-averaged spanwise

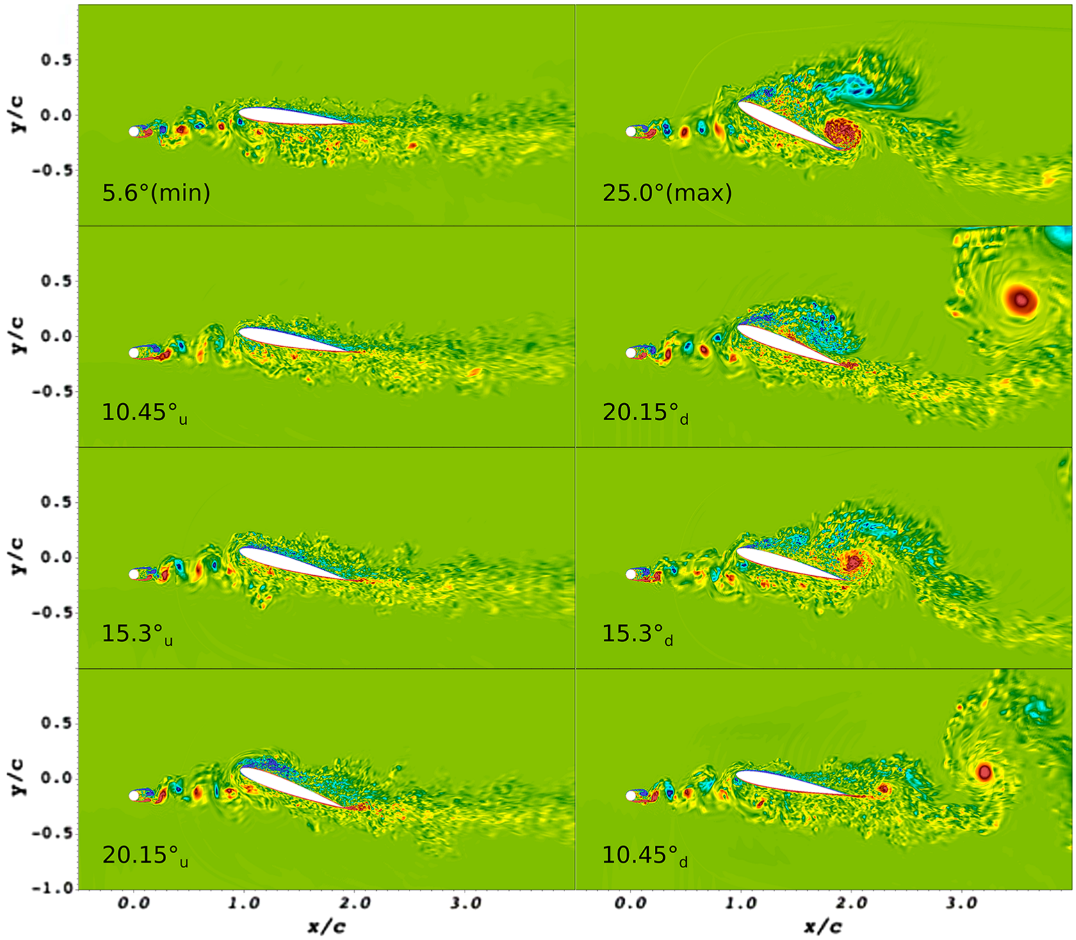

Fig. 13 **Zoomed-in spanwise-averaged spanwise vorticity plots of case 3 during the third cycle.**

vorticity (Figs. 12 and 13) for cases 2 and 3 shows evidence of a forming dynamic stall vortex in the 20.15°_u frames, though not as large as the DSV seen in the 20.15°_u frames of case 1 (Fig. 3). However, note that the forming DSV is larger in this frame for case 3 than in case 2. Thus, we see that the formation of the DSV occurs earliest for the steady freestream case resulting in the earliest detachment of the vortex and subsequent dynamic stall among the three cases, as also evidenced in Figs. 9 and 10. Again, because the disturbances in case 2 are larger upon the airfoil due to the cylinder's vertical alignment, the formation of the DSV occurs the latest among the three cases, leading to the latest occurrence of dynamic stall.

A comparison of the pressure coefficients along the suction side of the airfoils in all three cases (Fig. 14) again gives evidence of the timing of the DSV formation. The $\alpha = 20.15^\circ_u$ pressure profile plot shows that the DSV in case 1 is roughly at the half-chord distance (where the center of the vortex is determined by the lowest pressure values), the DSV is forming at the leading edge of the airfoil in case 2, and the DSV is roughly at the quarter-chord location in case 3. When the pitching airfoil begins its downstroke, a second major vortex is formed at the leading edge. The $\alpha = 20.15^\circ_d$ plots show evidence of the TEV in case 1 resulting from the detachment of the second major vortex, whereas the pressure values in case 2 show that the second major vortex is fairly weak and its center is located in front of the half-chord location, and in case 3, the center of the second major vortex is at about the three-quarter-chord location and appears to be much stronger than the vortex in case 2.

An indication of the strength of the DSV with respect to a specified volume can be obtained by performing a volume average of the spanwise vorticity over a cylindrical volume centered at the vortex center:

$$\Gamma_V \equiv \frac{\left| \int_{V_{\mathrm{cyl}}} \omega_z^* \, \mathrm{d}V_{\mathrm{cyl}} \right|}{V_{\mathrm{cyl}}} \tag{8}$$

where V_{cyl} is the volume of the cylinder being considered, and the nondimensional spanwise vorticity $\omega_z^* \equiv \omega_z U_\infty / c$. The center of the vortex is located by comparing the spanwise vorticity, streamwise velocity, and vertical velocity components in the spanwise-averaged fields. Because the vortices in each case have different radii, this measure indicates the concentration of vortex strength within the specified volume; thus, we use the term "volume strength". The volume strength of the DSV (Γ_V) is determined for all the three cases as the center reaches the $x/c = 1.95$ position in the flowfield, and integration is performed over a cylindrical volume with the radius of $r/c = 0.25$, as illustrated in Fig. 15 by the depicted circle, and the width $L_z/c = 0.2$, which corresponds to the span of the domain. Properties of the DSV in each of the cases as the center of the vortex reaches the $x/c = 1.95$ position in the flowfield is presented in Table 6. This comparison (Table 6) shows that the DSV is strongest in case 1, next strongest in case 3, and weakest

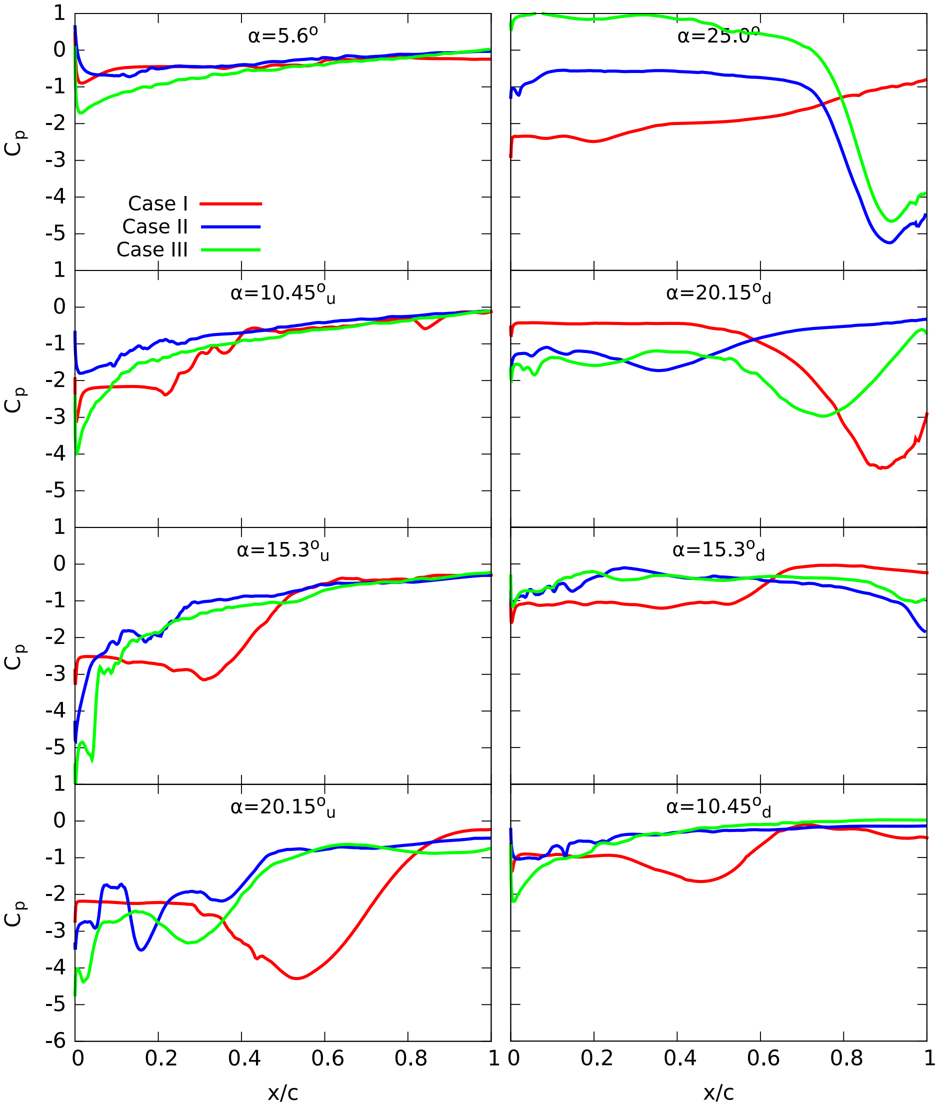

Fig. 14 Spanwise-averaged pressure coefficients along the suction surface of the airfoil for cases 1, 2, and 3 during the third cycle at angles of attack posted.

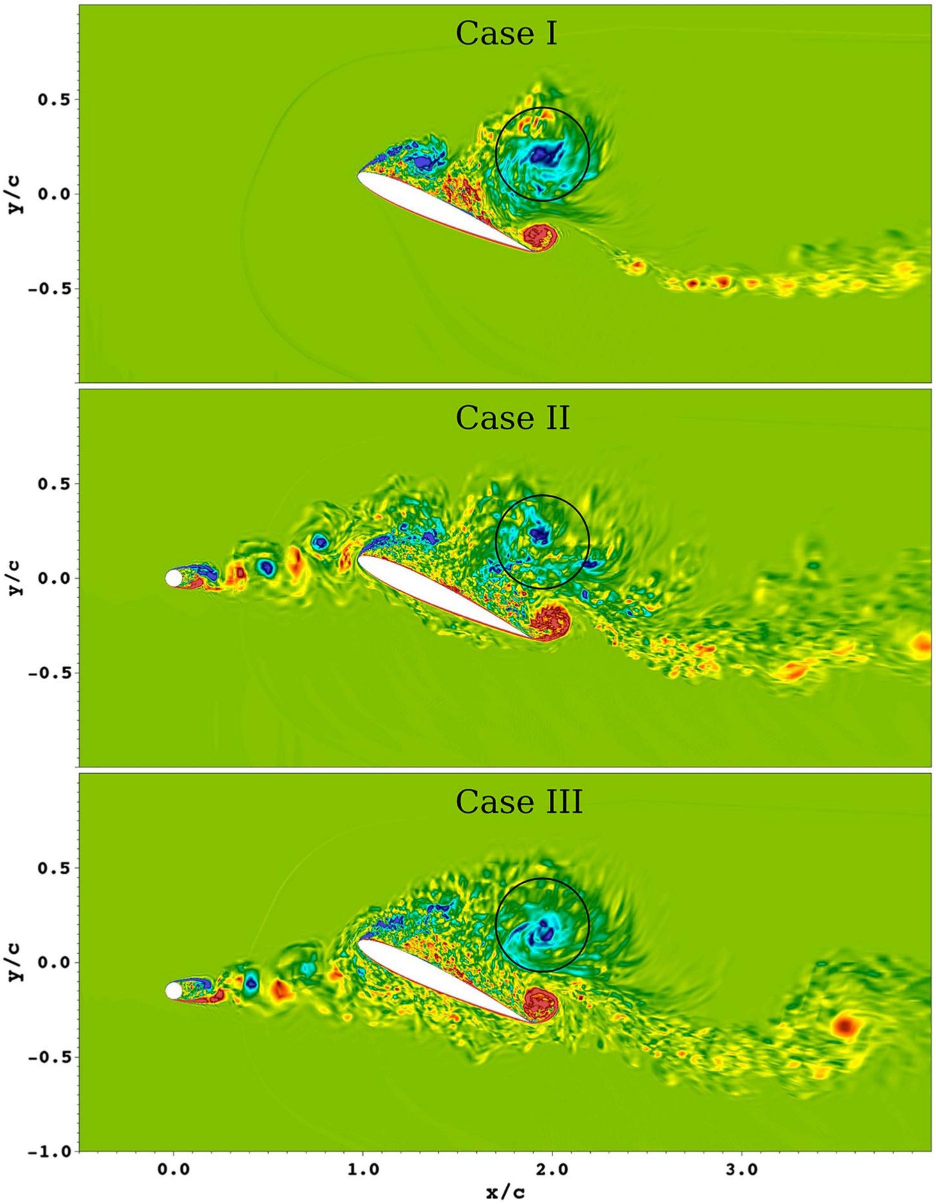

Fig. 15 Spanwise-averaged spanwise vorticity plots when the center of the DSV in the fourth cycle reaches the $x/c = 1.95$ position in the flowfield for all three cases.

in case 2, aligning with the pattern seen in most of the other results presented here.

Recall that previous results suggested that the DSV forms earlier in the pitching cycle for case 3 compared to case 2, yet note that the DSV in case 3 crosses the $x/c = 1.95$ position at a later time than the DSV in case 2. A possible explanation for this effect is as follows. In case 3, a strong counterclockwise rotating trailing-edge vortex forms early. As this TEV propagates upward, it creates a region with slower streamwise velocity in the downstream path of the DSV. This slower-moving fluid decreases the propagation speed of the DSV. This effect is also witnessed in the other cases, though the timings of the DSV and TEV formation do not produce a response that is as impactful. These timing differences are presumably due to the turbulent energy being concentrated in different regions of the flowfield. For example, in the 25° frame of Fig. 12, it appears that the disturbances created by the cylinder in case 2 play a larger role in the dynamics on the suction side of the airfoil, whereas in Fig. 13, we see that the turbulent interactions are concentrated on the pressure side of the airfoil at its maximum angle of attack.

Laminar-to-turbulent transition, separation, and reattachment of the airfoil boundary layer throughout the pitching cycle plays an important role in the physics of the dynamic stall. To characterize the state of the boundary-layer development throughout the pitching cycle, we plot phase-averaged values of skin friction coefficient along the airfoil suction surface for the three investigated cases in Fig. 16. Although a sudden growth of skin friction magnitude along

Table 6 Properties of the DSV during the third and fourth pitching cycles

Parameter	Case 1 (third cycle)	Case 1 (fourth cycle)	Case 2 (third cycle)	Case 2 (fourth cycle)	Case 3 (third cycle)	Case 3 (fourth cycle)
Vertical position y/c	0.240	0.208	0.146	0.187	0.168	0.199
Time tU_∞/c	47.8	67.1	48.4	68.0	48.7	68.4
Angle of attack α	24.19°_u	23.72°_u	24.77°_u	24.74°_u	24.93°_u	24.95°_u
Volume strength Γ	10.271	9.899	8.297	7.105	9.879	9.232

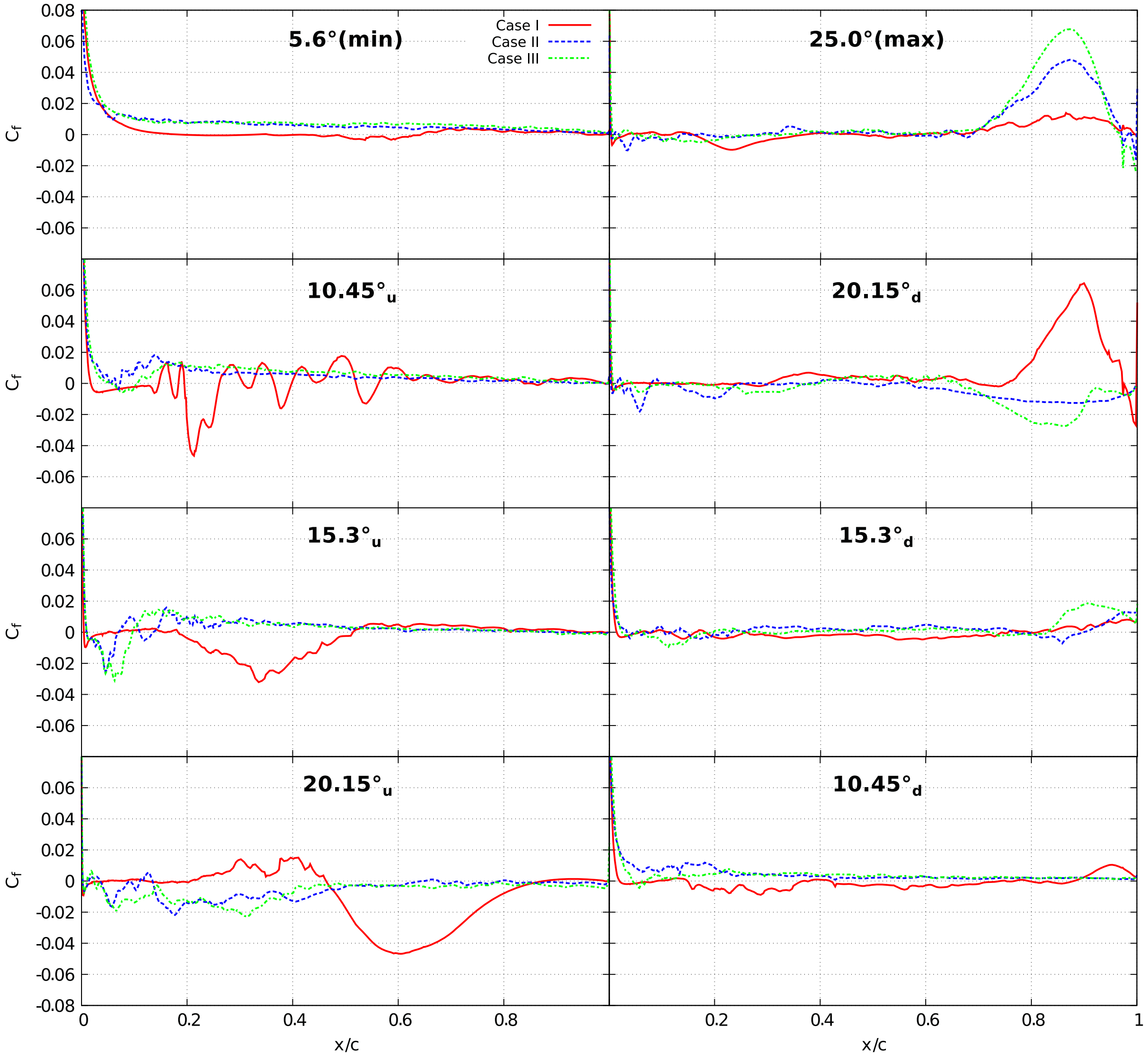

Fig. 16 Spanwise-averaged skin friction coefficients along the suction surface of the airfoil for cases 1, 2, and 3 phase averaged over the last five cycles at angles of attack posted.

the airfoil surface would indicate a laminar-to-turbulent transition, a negative sign of skin friction would point to the regions of the separated flow. In agreement with the previous observations, incoming wake turbulence seems to delay the formation of the vortical systems along the surface of the airfoil and subsequently delay the massive separation of the boundary layer during the upstroke which is significantly smaller and confined to the leading-edge region in cases 2 and 3. A large positive value of skin friction near the trailing edge at the maximum angle of attack 25 deg in cases 2 and 3 is associated with the presence of a strong trailing-edge vortex (stronger in case 3, as discussed previously), which in case 1 has already been formed and detached, whereas a signature of a secondary trailing-edge vortex is visible in case 1 at the downstroke angle 20.15°_d.

To complement the discussion of transition and instabilities, we show the three-dimensional turbulent flow structures at selected phases of the pitching cycle displayed by visualization of the λ_2 criterion in Fig. 17. For the undisturbed case 1, the evolution of unsteady flow structures is very similar to the dynamics described by Visbal [18] for a plunging airfoil motion at a similar Reynolds number and reduced frequency and by Mulleners and Raffel [35,36] for a pitching airfoil motion at a slightly higher Reynolds number and a similar reduced frequency. The dynamics can be characterized by initially laminar boundary layer with minor trailing-edge unsteadiness at $\alpha = 5.6$ deg, followed by a growth of a separated region and formation of a laminar shear layer. Subsequently, Kelvin–Helmoltz instabilities emerge that result into a shear layer roll-up into multiple vortices at $\alpha = 10.45^\circ_u$. This is followed by a sinusoidal (spanwise) instability and a massive shear-layer breakdown at $\alpha = 15.3^\circ_u$ that forms a dynamic stall vortex visible at $\alpha = 20.15^\circ_u$. The DSV then propagates along the airfoil surface and detaches by $\alpha = 25$ deg, while subsequently the flow reattaches and boundary layer relaminarizes during the downstroke. The dynamics for the turbulent wake inflow cases 2 and 3 is, however, drastically different. The first observation is the absence of the laminar shear layer at the beginning of the cycle due to the boundary layers being turbulent even at smallest angles of attack. Comparing with the vortex dynamics in Figs. 12 and 13, it can be seen that the wake vortices shed by the cylinder break down into smaller-scale structures by the pitching airfoil surface and trip the boundary layers early in the cycle. Because of the absence of strong shear layers, the Kelvin–Helmoltz instabilities are suppressed; shear-layer vortices are formed later, are weaker, and are confined to the leading-edge region of the airfoil; and shear-layer roll-up and separation are delayed and diminished in strength, which results in a weaker dynamic stall vortex and weaker secondary vortex systems. Also, boundary layers stay turbulent and do not seem to relaminarize at the downstroke. Case 3, as opposed to case 2, also features strong turbulent flow on the pressure side of the airfoil, which potentially explains stronger trailing-edge vortices in this case.

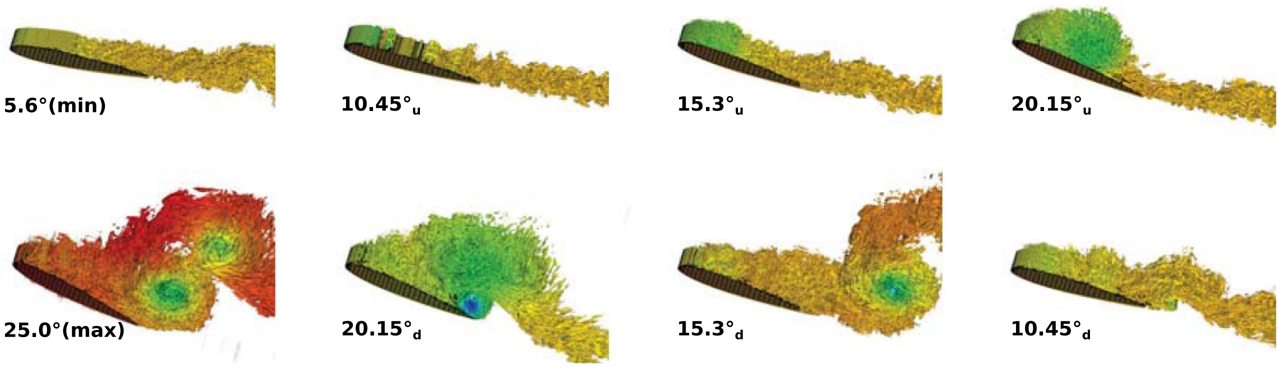

a) Case I

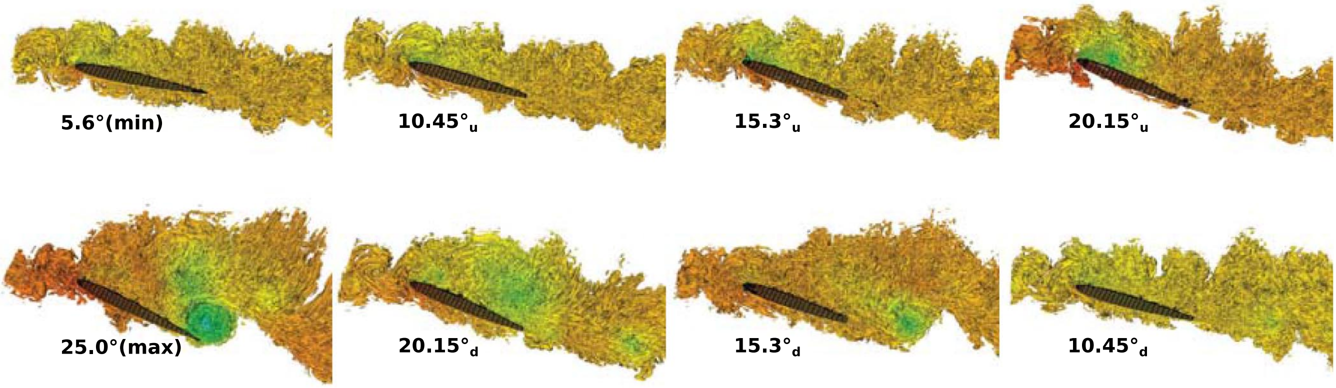

b) Case II

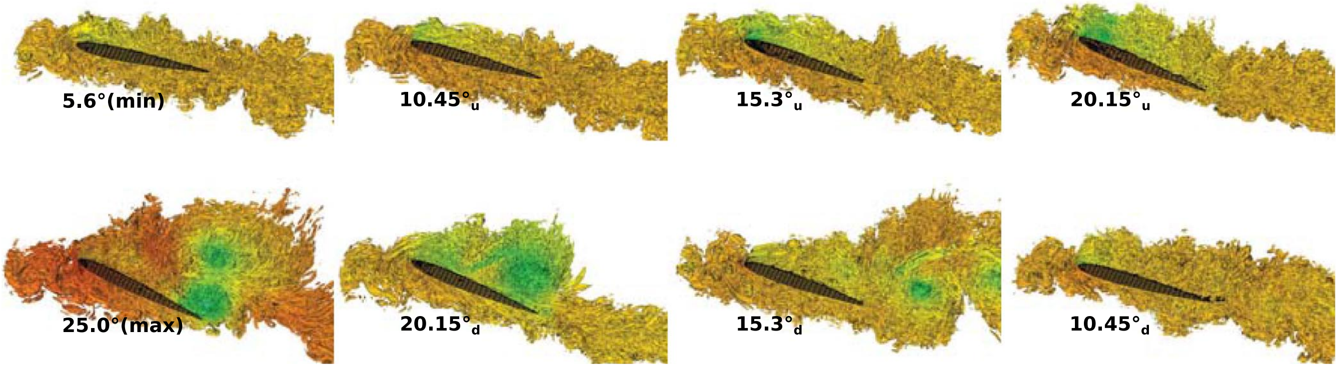

c) Case III

Fig. 17 Pressure pseudocolor projected onto the $\lambda_2 = -0.1$ isosurface during the sixth pitching cycle. The black grid is used to outline the airfoil and is not a representation of the computational mesh.

V. Power Spectral Densities of Aerodynamic Coefficients

The power spectral density (PSD) functions of the lift, drag, and pitching moment coefficients are computed by importing the aerodynamic data into the periodogram power spectral density estimate function in MATLAB. The aerodynamic coefficients were calculated within the moving overlapping mesh simulation at nondimensional time intervals of $\Delta t U_\infty / c = 0.05$, and PSD functions were calculated from data collected in pitching cycles 2 through 6, with cycle 1 being excluded because the turbulent wake is not fully developed at the beginning of the simulation.

Figure 18 gives a side-by-side comparison of the PSD function plots for lift, drag, and pitching moment coefficients respectively. As we expect, the dominant frequency peak in every case corresponds with the pitching frequency of the airfoil, which shows that most of energy that is transferred to the airfoil occurs near this frequency that was imposed upon the system. In the lift plots (Fig. 18), both cases 2 and 3 show another power peak corresponding with the vortex-shedding frequency of the upstream cylinder (indicated by dashed lines), suggesting that a moderate amount of energy affecting the lift acting on the airfoil is transferred by the turbulent wake. Note, however, that the peak at the cylinder vortex-shedding frequency is not as prominent in case 3, likely due to the fact that the turbulent wake is not directly incident upon the airfoil's leading edge. Each of the case 2 PSD function plots display this secondary peak, though in the case of the pitching moment coefficient, it is not quite as pronounced, indicating that the higher-frequency energy contributions from the upstream cylinder's wake are not as crucial to the pitching moment experienced by the airfoil as the forced pitching frequency imposed upon it.

In contrast, there are no noticeable peaks resulting from the upstream cylinder's wake in the drag and pitching moment PSD function plots for case 3. This suggests that the energy transferred to the airfoil due to the pitching frequency plays a much more important role in the determination of the drag force and pitching moment experienced by the airfoil in case 3. All of this additionally indicates

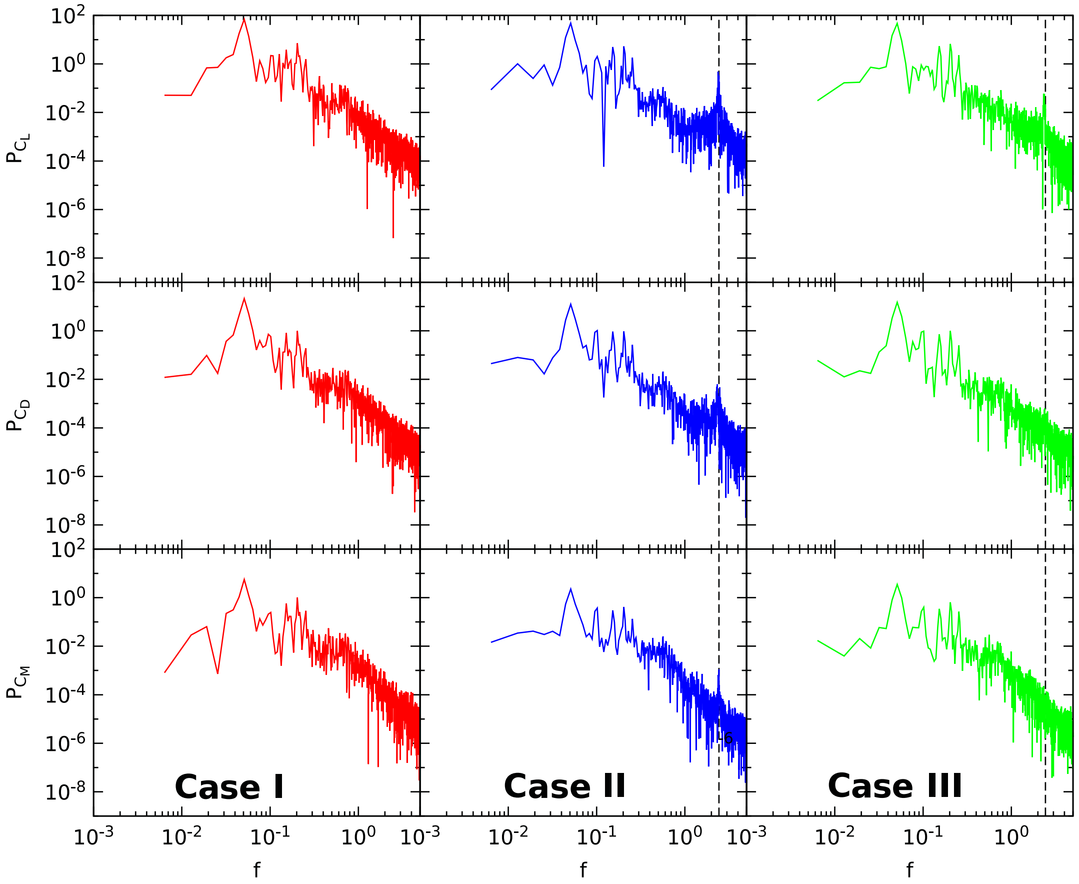

Fig. 18 PSD functions of the lift, drag, and pitching moment coefficients for the three cases. The dashed lines in applicable plots designate the vortex-shedding frequency of the upstream cylinder.

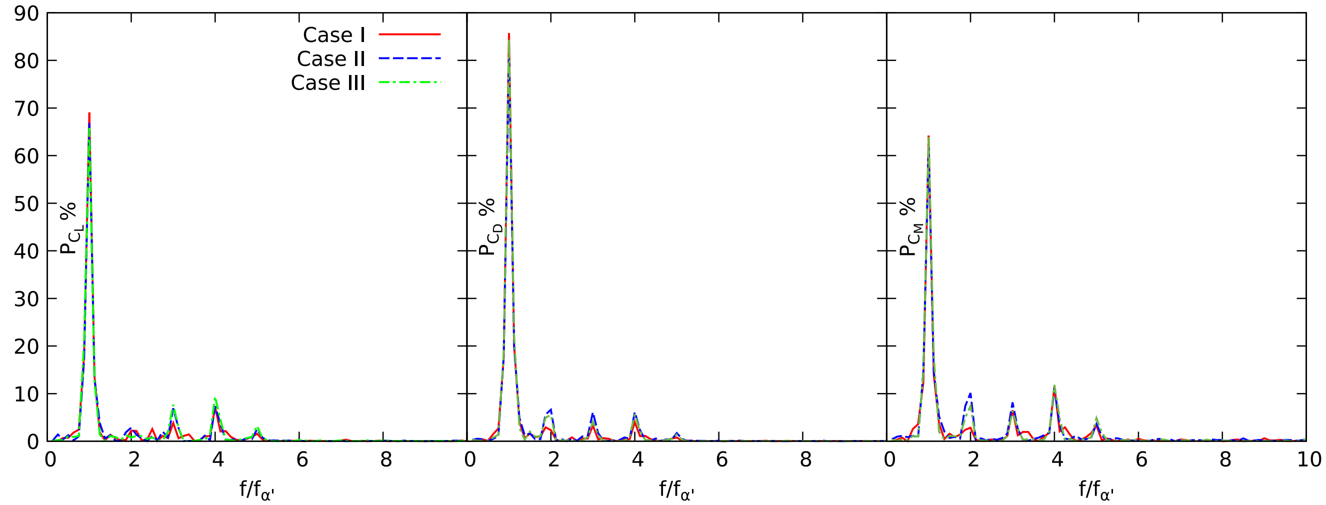

Fig. 19 PSD functions of aerodynamic coefficients. Power is normalized by the total power of the function within the frequency range examined, and frequency by the pitching frequency of the airfoil.

that a turbulent wake incident upon the leading edge of a pitching airfoil is likely to play a larger role in the forces and moments acting on the airfoil than in the case with the same turbulent wake but incident upon the pressure side of the pitching airfoil, which is consistent with the previous discussion.

Following the normalization procedure employed in [69], we now focus on the lower-frequency region of the PSD function plots. In Fig. 19, the frequency is normalized by the pitching frequency of the airfoil ($f = f/f_{\alpha'}$), so that "1" now represents the pitching frequency. Additionally, the PSD function is normalized by the total power in the full range of frequencies computed,

$$P\Big/\int_0^\infty P(f)\,\mathrm{d}f$$

allowing for more direct comparison of PSD functions among the three cases. The frequencies lower than $f/f_{\alpha'} = 10$ are displayed in Fig. 19, where we clearly see higher-order harmonics in every case that are prominent until about the fifth harmonic. In general, the peaks at the pitching frequency and at the harmonics correspond quite nicely among the three cases, though slight differences are apparent. In all of the plots, the peaks at the harmonics are generally larger in

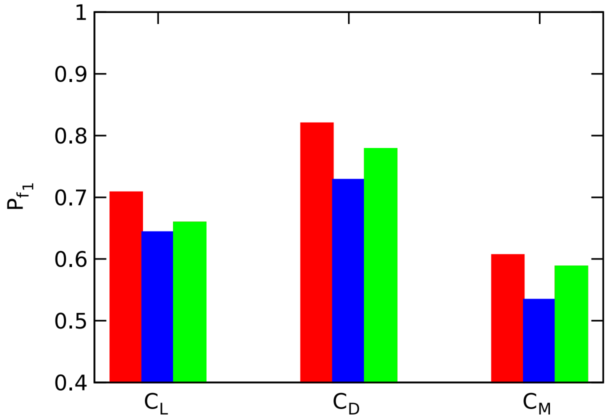

Fig. 20 Energy partition derived from the aerodynamic coefficient PSD functions at the airfoil pitching frequency for cases 1 (red, leftmost bars), 2 (blue, center bars), and 3 (green, rightmost bars).

cases 2 and 3 than in case 1. The harmonics, as discussed in [69], indicate that there is a nonlinear interaction between the pitching airfoil and the fluid, which transfers energy from the pitching frequency to the harmonics, whereas larger harmonics denote more prevalent nonlinear interactions.

In each of the plots, the PSD function at the airfoil pitching frequency is largest for case 1. The main peaks of cases 2 and 3 in the PSD plot of C_L lie almost directly on top of each other. We calculate the energy partition at the pitching frequency to achieve a more clear indication of the prominence of nonlinear interactions in each case [69]. The energy partition at the pitching frequency is calculated by

$$P_{f_1} = \frac{\int_{0.5}^{1.5} P(f)\,\mathrm{d}f}{\int_0^{\infty} P(f)\,\mathrm{d}f} \tag{9}$$

where a value of "1" would indicate the absence of nonlinear interactions or that all of the energy lies at the fundamental frequency. Thus, we should expect that nonlinear interactions would be greater in a system that introduces an upstream wake turbulence as we do in cases 2 and 3, indicated by lower energy partition values at the pitching frequency. Figure 20 displays the energy partition values at the airfoil pitching frequency for the forces and moments in all three cases. We see, in fact, that the values at this energy partition are greater for case 1 than for the other cases, and case 3 is greater than case 2 in every case, though only slightly for C_L. This implies that the greatest nonlinear interactions occur in case 2, where the wake turbulence is more concentrated on the suction side of the airfoil (where the DSV vortices form), followed by case 3, where the wake turbulence is more prominent on the pressure side of the airfoil, with nonlinear interactions playing the smallest role in case 1 performed in the absence of an upstream wake. Also note that nonlinear interactions appear to play the largest role in the moments experienced by the airfoil (indicated by the lowest energy partition values), which corresponds well with the results displayed in the C_M plot of Fig. 10 that shows major reductions in the magnitude of pitching moment throughout nearly the entire cycle when the pitching airfoil is in the presence of a turbulent wake.

VI. Conclusions

Direct numerical simulations of a flow around a pitching airfoil were performed in a turbulent wake shed by an upstream cylinder for a Reynolds number of $Re_c = 44{,}000$. A turbulent wake incident upon a pitching airfoil largely affects the forces and moments acting on the airfoil, and the flow structure of the fluid, including vortex formation. For the conditions investigated, dynamic stall of a pitching airfoil occurs at a later time (and larger angle of attack) when in the presence of a turbulent wake, due to the delayed formation, and thus detachment, of the dynamic stall vortex (DSV). In addition, the weakening of the DSV by the wake turbulence is also observed as measured by the normalized value of the circulation around the vortex. Consequently, the lift, drag, and pitching moment coefficient curves display phase shifts in the stall events, and the magnitude of the peak values is also reduced during both the upstroke and the downstroke; this effect can be seen in both instantaneous and cycle-averaged values. The reduction is highest for the pitching moment and the drag and is relatively small for the lift coefficient. A signature of the wake vortices shed from the upstream cylinder is seen in the spectra of time series of the aerodynamic coefficients, especially lift, as distinct peaks corresponding to the Strouhal frequency of the cylinder.

The analysis of spanwise vorticity, three-dimensional turbulent structures visualized by the λ_2 criterion, and phase-averaged skin friction coefficient values in the current direct numerical simulations data suggests that the effect of an upstream wake turbulence impinging on the airfoil is to weaken the formation of unsteady vortical systems associated with the dynamic stall process and to delay the boundary-layer separation. Similar effects of freestream turbulence were reported in the previous literature, attributed to early laminar-to-turbulent transition in the boundary layer [23], early laminar-to-turbulent transition and enhanced momentum transfer in the shear layer separating from the leading edge [25,29], and breakdown of the separation bubble by the upstream turbulence [26]. The present observations suggest the evidence of at least first two of the aforementioned phenomena that lead to a suppression of a distinct shear-layer formation, subsequent shear-layer instabilities, and flow separation and result in weakened dynamic stall vortices that, according to [18,35,36], arise from these instabilities and a flow separation.

Although the two major effects of freestream turbulence are associated with a suppression of flow separation and airfoil vortical systems, it is understandable that manifestation of these two major effects on the values of the lift, drag, and pitching moment can be different depending on a dynamic stall scenario. To illustrate this, it is noted that, although dynamic stall delay was observed in the studies [25,29] and in the current study, no stall delay was found in [23,24,26]. Additionally, Conger and Ramaprian [23] reported a significant increase in lift throughout the airfoil pitch-up, whereas the other investigators found little or no effect on lift during the pitch-up [24,26] or a slight decrease [29] (and the current study). Also, increased values of the aerodynamic coefficients during pitch-down were reported in [24,26] as opposed to decreased values in the current study. It is reasonable to conclude that the exact manner in which aerodynamic performance is affected by the freestream turbulence must be related to the mode of a dynamic stall in a corresponding undisturbed flow regime. Several investigators showed the difference between a light stall (stall related to a trailing-edge separation) and a deep stall (stall associated with the formation and detachment of the dynamic stall vortex) in a dynamic stall problem [15,35]. In a light stall, the airfoil motion parameters are such that the downstroke begins before the dynamic stall vortex had time to fully form and detach, whereas in a deep stall, at least one or sometimes many major vortical systems form and detach throughout the cycle. In the present study, a deep stall was experienced, and the current results clearly showed that the effect of incoming turbulence during deep stall is to decrease the lift and other coefficients due to the weakening of the dynamic stall vortical systems before detachment. It is, again, reasonable to conclude that, during the light stall associated with the flow separation, the effect of turbulence would be to increase the lift due to the reduction of the separation bubble, which would explain the findings in [23,24,26]. In addition, the relative timing of the formation and detachment of the DSV and TEV vortices in the pitching cycle in the baseline case will presumably affect the manner in which the unsteady flow processes and the corresponding aerodynamic forces and moments will be affected by the incoming turbulence. The mode of the dynamic stall depends on many parameters, such as Reynolds number, pitch amplitude, pitch frequency, and airfoil geometry [10]. Depending on these parameters, the detailed manner in which the turbulence will influence the airfoil aerodynamics will differ, although the root of the modifications will stem from the common nature of weakening of the separated flow and of the unsteady vortex systems by the turbulence. A strong influence of turbulence on the details of the dynamic stall has an implication that it is exceptionally difficult to achieve close agreement between experimental and numerical results in these unsteady flows because even a slight level of turbulence in the experimental system will affect the data. Another degree of uncertainty when comparing with the experimental data is the blockage effect, which is not modeled numerically. Further investigations of the effect of blockage on the unsteady aerodynamics are needed to provide a proper guidance on the expectations when comparing experiments and simulations in these sensitive systems.

The present study revealed that the magnitude of drag and pitching moments can be significantly reduced for most of the pitching cycle with the presence of an upstream wake turbulence. Reduction in mean drag leads to higher efficiencies of cyclic operations, such as in rotary-wing flight and wind-turbine power production. Lower pitching moments additionally imply a decrease in a structural strain on dynamically pitching blades and wings, potentially improving the lifespan of these mechanical systems. Weaker dynamic stall vortices shed from the airfoil in disturbed upstream flow could lead to less intrusive vortex interactions with downstream structures, as in the case of a blade–vortex interaction. These findings hold promise for potentially successful flow control strategies in unsteady environments.

Acknowledgments

We would like to acknowledge support for this work given by the National Science Foundation (NSF) grant Division of Civil, Mechanical and Manufacturing Innovation-1250124 and thank the NSF Extreme Science and Engineering Discovery Environment program for providing the computational resource allocation on the San Diego Supercomputer Center Comet and Texas Advanced Computing Center Stampede clusters where the simulations were performed.

References

[1] Ham, N., and Garelick, M., "Dynamic Stall Considerations in Helicopter Rotors," *Journal of the American Helicopter Society*, Vol. 13, No. 2, 1968, pp. 49–55. doi:10.4050/JAHS.13.49

[2] Pierce, G., Kunz, D., and Malone, J., "The Effect of Varying Freestream Velocity on Airfoil Dynamic Stall Characteristics," *Journal of the American Helicopter Society*, Vol. 23, No. 2, 1978, pp. 27–33. doi:10.4050/JAHS.23.27

[3] Larsen, J., Nielsen, S., and Krenk, S., "Dynamic Stall Model for Wind Turbine Airfoils," *Journal of Fluids and Structures*, Vol. 23, No. 7, 2007, pp. 959–982. doi:10.1016/j.jfluidstructs.2007.02.005

[4] Brady, W., and Ludwig, G., "Unsteady Stall of Axial Flow Compressors," Cornell Aeronautical Lab Inc. Rept. AM-1762-A-1, Buffalo, NY, 1963.

[5] Shi, Z.-W., and Ming, X., "Effects of Unsteady Freestream on Aerodynamic Characteristics of a Pitching Delta Wing," *Journal of Aircraft*, Vol. 45, No. 6, 2008, pp. 2182–2185. doi:10.2514/1.38925

[6] Shi, Z., and Ming, X., "Experimental Investigation on a Pitching Motion Delta Wing in Unsteady Free Stream," *Modern Physics Letters B*, Vol. 23, No. 3, 2009, pp. 409–412. doi:10.1142/S0217984909018527

[7] McCroskey, W., Carr, L., and McAlister, K., "Dynamic Stall Experiments on Oscillating Airfoils," *AIAA Journal*, Vol. 14, No. 1, 1976, pp. 57–63. doi:10.2514/3.61332

[8] McCroskey, W., "Unsteady Airfoils," *Annual Review of Fluid Mechanics*, Vol. 14, 1982, pp. 285–311. doi:10.1146/annurev.fl.14.010182.001441

[9] Ericsson, L., and Reding, J., "Fluid Dynamics of Unsteady Separated Flow. Part 2. Lifting Surfaces," *Progress in Aerospace Sciences*, Vol. 24, No. 4, 1987, pp. 249–356. doi:10.1016/0376-0421(87)90001-7

[10] Carr, L., "Progress in Analysis and Prediction of Dynamic Stall," *Journal of Aircraft*, Vol. 25, No. 1, 1988, pp. 6–17. doi:10.2514/3.45534

[11] Visbal, M., "On Some Physical Aspects of Airfoil Dynamic Stall," *Proceedings of the International Symposium on Non-Unsteady Fluid Dynamics*, edited by J. Miller, and D. Telionis, Vol. 92, The American Soc. of Mechanical Engineers, New York, 1990.

[12] Carr, L. W., and Chandrasekhara, M., "Compressibility Effects on Dynamic Stall," *Progress in Aerospace Sciences*, Vol. 32, No. 6, 1996, pp. 523–573. doi:10.1016/0376-0421(95)00009-7

[13] Ekaterinaris, J., and Platzer, M., "Computational Prediction of Airfoil Dynamic Stall," *Progress in Aerospace Sciences*, Vol. 33, No. 11, 1998, pp. 759–846. doi:10.1016/S0376-0421(97)00012-2

[14] Carr, L., McAlister, K., and McCroskey, W., "Analysis of the Development of Dynamic Stall Based on Oscillating Airfoil Experiments," NASA TN D-8382, 1977.

[15] McCroskey, W., "The Phenomenon of Dynamic Stall," National Aeronautics and Space Administration NASA-A-8464, Ames Research Center, Moffett Field, CA, 1981.

[16] Ericsson, L., and Reding, J., "Fluid Mechanics of Dynamic Stall Part 1. Unsteady Flow Concepts," *Journal of Fluids and Structures*, Vol. 2, No. 1, 1988, pp. 1–33. doi:10.1016/S0889-9746(88)90116-8

[17] Choudhuri, P., and Knight, D., "Effects of Compressibility, Pitch Rate, and Reynolds Number on Unsteady Incipient Leading-Edge Boundary Layer Separation over a Pitching Airfoil," *Journal of Fluid Mechanics*, Vol. 308, Feb. 1996, pp. 195–217. doi:10.1017/S0022112096001450

[18] Visbal, M., "Numerical Investigation of Deep Dynamic Stall of a Plunging Airfoil," *AIAA Journal*, Vol. 49, No. 10, 2011, pp. 2152–2170. doi:10.2514/1.J050892

[19] Garmann, D., and Visbal, M., "Numerical Investigation of Transitional Flow over a Rapidly Pitching Plate," *Physics of Fluids*, Vol. 23, No. 9, 2011, Paper 094106. doi:10.1063/1.3626407

[20] Kottapalli, S., and Pierce, G., "Drag on an Oscillating Airfoil in a Fluctuating Free Stream," *Journal of Fluids Engineering*, Vol. 101, No. 3, 1979, pp. 391–399. doi:10.1115/1.3448985

[21] Gharali, K., and Johnson, D., "Dynamic Stall Simulation of a Pitching Airfoil Under Unsteady Freestream Velocity," *Journal of Fluids and Structures*, Vol. 42, Oct. 2013, pp. 228–244. doi:10.1016/j.jfluidstructs.2013.05.005

[22] Gharali, K., and Johnson, D., "Effects of Nonuniform Incident Velocity on a Dynamic Wind Turbine Airfoil," *Wind Energy*, Vol. 18, No. 2, Feb. 2014, pp. 237–251.

[23] Conger, R., and Ramaprian, B., "Pressure Measurements on a Pitching Airfoil in a Water Channel," *AIAA Journal*, Vol. 32, No. 1, 1994, pp. 108–115. doi:10.2514/3.11957

[24] Amandolèse, X., and Széchényi, E., "Experimental Study of the Effect of Turbulence on a Section Model Blade Oscillating in Stall," *Wind Energy*, Vol. 7, No. 4, 2004, pp. 267–282. doi:10.1002/we.v7:4

[25] Leu, T., Yu, J., Hu, C., Miau, J., Liang, S., Li, J., Cheng, J., and Chen, S., "Experimental Study of Free Stream Turbulence Effects on Dynamic Stall of Pitching Airfoil by Using Particle Image Velocimetry," *Applied Mechanics and Materials*, Vol. 225, Nov. 2012, pp. 103–108. doi:10.4028/www.scientific.net/AMM.225

[26] Kim, Y., and Xie, Z.-T., "Modelling the Effect of Freestream Turbulence on Dynamic Stall of Wind Turbine Blades," *Computers and Fluids*, Vol. 129, April 2016, pp. 53–66. doi:10.1016/j.compfluid.2016.02.004

[27] Xie, Z., and Castro, I., "Efficient Generation of Inflow Conditions for Large Eddy Simulation of Street-Scale Flows," *Flow, Turbulence and Combustion*, Vol. 81, No. 3, 2008, pp. 449–470. doi:10.1007/s10494-008-9151-5

[28] Tennekes, H., and Lumley, J., *A First Course in Turbulence*, MIT Press, Cambridge, MA, 1972, pp. 104–145.

[29] Chen, J., and Choa, C.-C., "Freestream Disturbance Effects on an Airfoil Pitching at Constant Rate," *Journal of Aircraft*, Vol. 36, No. 3, 1999, pp. 507–514. doi:10.2514/2.2485

[30] Sayadi, T., Hamman, C., and Moin, P., "Direct Numerical Simulation of Complete H-Type and K-Type Transitions with Implications for the Dynamics of Turbulent Boundary Layers," *Journal of Fluid Mechanics*, Vol. 724, June 2013, pp. 480–509. doi:10.1017/jfm.2013.142

[31] Wu, X., and Moin, P., "Direct Numerical Simulation of Turbulence in a Nominally Zero-Pressure-Gradient Flat-Plate Boundary Layer,"

Journal of Fluid Mechanics, Vol. 630, July 2009, pp. 5–41. doi:10.1017/S0022112009006624

[32] Ovchinnikov, V., Piomelli, U., and Choudhari, M., "Numerical Simulations of Boundary-Layer Transition Induced by a Cylinder Wake," *Journal of Fluid Mechanics*, Vol. 547, Jan. 2006, pp. 413–441. doi:10.1017/S0022112005007342

[33] Lee, T., and Gerontakos, P., "Investigation of Flow over an Oscillating Airfoil," *Journal of Fluid Mechanics*, Vol. 512, Aug. 2004, pp. 313–341. doi:10.1017/S0022112004009851

[34] Visbal, M., "High-Fidelity Simulation of Transitional Flows Past a Plunging Airfoil," *AIAA Journal*, Vol. 47, No. 11, 2009, pp. 2685–2697. doi:10.2514/1.43038

[35] Mulleners, K., and Raffel, M., "The Onset of Dynamic Stall Revisited," *Experiments in Fluids*, Vol. 52, No. 3, 2012, pp. 779–793. doi:10.1007/s00348-011-1118-y

[36] Mulleners, K., and Raffel, M., "Dynamic Stall Development," *Experiments in Fluids*, Vol. 54, No. 2, 2013, p. 1469. doi:10.1007/s00348-013-1469-7

[37] Merrill, B., and Peet, Y., "Effects of Upstream Disturbances on a Pitching NACA0012 Airfoil," *54th Aerospace Sciences Meeting*, AIAA Paper 2016-1308, Jan. 2016.

[38] Wu, X., "Inflow Turbulence Generation Methods," *Annual Review of Fluid Mechanics*, Vol. 49, 2017, pp. 23–49. doi:10.1146/annurev-fluid-010816-060322

[39] Lee, S., Lele, S., and Moin, P., "Simulation of Spatially Evolving Turbulence and Applicability of Taylor's Hypothesis in Compressible Flow," *Physics of Fluids A*, Vol. 4, No. 7, 1992, pp. 1521–1530. doi:10.1063/1.858425

[40] Ovchinnikov, V., Piomelli, U., and Choudhari, M., "Inflow Conditions for Numerical Simulation of Bypass Transition," *42nd AIAA Aerospace Sciences Meeting and Exhibit*, AIAA Paper 2004-0591, 2004.

[41] Kim, J., Moin, P., and Moser, R., "Turbulence Statistics in Fully Developed Channel Flow at Low Reynolds Number," *Journal of Fluid Mechanics*, Vol. 177, April 1987, pp. 133–166. doi:10.1017/S0022112087000892

[42] Lund, T., Wu, X., and Squires, K., "Generation of Turbulent Inflow Data for Spatially-Developing Boundary Layer Simulations," *Journal of Computational Physics*, Vol. 140, No. 2, 1998, pp. 233–258. doi:10.1006/jcph.1998.5882

[43] Keating, A., Piomelli, U., and Balaras, E., "A Priori and A Posteriori Tests of Inflow Conditions for Large-Eddy Simulation," *Physics of Fluids*, Vol. 16, No. 12, 2004, pp. 4696–4712. doi:10.1063/1.1811672

[44] Merrill, B., Peet, Y., Fischer, P., and Lottes, J., "A Spectrally Accurate Method for Overlapping Grid Solution of Incompressible Navier–Stokes Equations," *Journal of Computational Physics*, Vol. 307, Feb. 2016, pp. 60–93. doi:10.1016/j.jcp.2015.11.057

[45] Merril, B., and Peet, Y., "High-Order Moving Overlapping Grid Methodology for Aerospace Applications," *53rd AIAA Aerospace Sciences Meeting*, AIAA Paper 2015-1743, Jan. 2015.

[46] Merrill, B., and Peet, Y., "Moving Overlapping Grid Methodology of Spectral Accuracy for Incompressible Flow Solutions Around Rigid Bodies in Motion," *Journal of Computational Physics*, 2016 (submitted).

[47] Panda, J., and Zaman, K., "Experimental Investigation of the Flow Field of an Oscillating Airfoil and Estimation of Lift from Wake Surveys," *Journal of Fluid Mechanics*, Vol. 265, April 1994, pp. 65–95. doi:10.1017/S0022112094000765

[48] Reynolds, W. C., "The Potential and Limitations of Direct and Large Eddy Simulations," *Lecture Notes in Physics*, Vol. 357, edited by J. L. Lumlery, Springer–Verlag, Berlin, 1990, pp. 313–343.

[49] Fischer, P., Lottes, J., and Kerkemeier, S., "Nek5000," Argonne National Lab., Argonne, IL, 2015, http://nek5000.mcs.anl.gov [retrieved Nov. 2016].

[50] Deville, M., Fischer, P., and Mund, E., *High-Order Methods for Incompressible Fluid Flow*, Vol. 9, Cambridge Univ. Press, Cambridge, U.K., 2002, pp. 234–325.

[51] Karniadakis, G., and Sherwin, S., *Spectral/hp Element Methods for Computational Fluid Dynamics*, Oxford Univ. Press, New York, 2013, pp. 59–61,207–210,222–224.

[52] Hirt, C., Amsden, A., and Cook, J., "An Arbitrary Lagrangian–Eulerian Computing Method for All Flow Speeds," *Journal of Computational Physics*, Vol. 14, No. 3, 1974, pp. 227–253. doi:10.1016/0021-9991(74)90051-5

[53] Hughes, T., Liu, W., and Zimmermann, T., "Lagrangian–Eulerian Finite Element Formulation for Incompressible Viscous Flows," *Methods in Applied Mechanics and Engineering*, Vol. 29, No. 3, 1981, pp. 329–349. doi:10.1016/0045-7825(81)90049-9

[54] Visbal, M., and Gaitonde, D., "On the Use of High-Order Finite Difference Schemes on Curvilinear and Deforming Meshes," *Journal of Computational Physics*, Vol. 181, No. 1, 2002, pp. 155–185. doi:10.1006/jcph.2002.7117

[55] Ekaterinaris, J., Cricelli, A., and Platzer, M., "A Zonal Method for Unsteady, Viscous, Compressible Airfoil Flows," *Journal of Fluids Structures*, Vol. 8, No. 1, 1994, pp. 107–123. doi:10.1006/jfls.1994.1005

[56] Peet, Y., and Fischer, P., "Stability Analysis of Interface Temporal Discretization in Grid Overlapping Methods," *SIAM Journal on Numerical Analysis*, Vol. 50, No. 6, 2012, pp. 3375–3401. doi:10.1137/110831234

[57] Pope, S. B., *Turbulent Flows*, Cambridge Press, Cambridge, U.K., 2000, pp. 182–189.

[58] Bisplinghoff, R., Ashley, H., and Halfman, R., *Aeroelasticity*, Courier, Mineola, NY, 2013, pp. 251–280.

[59] Merrill, B., "High-Order Moving Overlapping Grid Methodology in a Spectral Element Method," Ph.D. Thesis, Arizona State Univ., Tempe, AZ, 2016.

[60] Beaudan, P., and Moin, P., "Numerical Experiments on the Flow Past a Circular Cylinder at Sub-Critical Reynolds Number," Stanford Univ. Rept. TF-62, Thermosciences Division, Stanford, CA, 1994.

[61] Mittal, R., and Moin, P., "Suitability of Upwind-Biased Finite Difference Schemes for Large-Eddy Simulation of Turbulent Flows," *AIAA Journal*, Vol. 35, No. 8, 1997, pp. 1415–1417. doi:10.2514/2.253

[62] Parnaudeau, P., Carlier, J., Heitz, D., and Lamballais, E., "Experimental and Numerical Studies of the Flow over a Circular Cylinder at Reynolds Number 3900," *Physics of Fluids*, Vol. 20, No. 8, 2008, Paper 085101. doi:10.1063/1.2957018

[63] Kravchenko, A., and Moin, P., "Numerical Studies of Flow over a Circular Cylinder at $Re_D = 3900$," *Physics of Fluids*, Vol. 12, No. 2, 2000, pp. 403–417. doi:10.1063/1.870318

[64] Ma, X., Karamanos, G.-S., and Karniadakis, G., "Dynamics and Low-Dimensionality of a Turbulent Near Wake," *Journal of Fluid Mechanics*, Vol. 410, May 2000, pp. 29–65. doi:10.1017/S0022112099007934

[65] Ong, L., and Wallace, J., "The Velocity Field of the Turbulent Very Near Wake of a Circular Cylinder," *Experiments in Fluids*, Vol. 20, No. 6, 1996, pp. 441–453. doi:10.1007/BF00189383

[66] Cardell, G., "Flow Past a Circular Cylinder with a Permeable Wake Splitter Plate," Ph.D. Thesis, California Inst. of Technology, Pasadena, CA, 1993.

[67] Cimbala, J., Nagib, H., and Roshko, A., "Large Structure in the Far Wakes of Two-Dimensional Bluff Bodies," *Journal of Fluid Mechanics*, Vol. 190, May 1988, pp. 265–298. doi:10.1017/S0022112088001314

[68] Dynnikova, J., Dynnikov, Y., and Guvernyuk, S., "Mechanism Underlying Karman Vortex Street Breakdown Preceding Secondary Vortex Street Formation," *Physics of Fluids*, Vol. 28, No. 5, 2016, Paper 054101. doi:10.1063/1.4947449

[69] Tsang, K., So, R., Leung, R., and Wang, X., "Dynamic Stall Behavior from Unsteady Force Measurements," *Journal of Fluids and Structures*, Vol. 24, No. 1, 2008, pp. 129–150. doi:10.1016/j.jfluidstructs.2007.06.007

S. Fu
Associate Editor